International Journal of Mechanical Sciences 267 (2024) 108971

Contents lists available at ScienceDirect

International Journal of Mechanical Sciences

journal homepage: www.elsevier.com/locate/ijmecsci

Modelling of grain size effects in progressive microforming using CPFEM

Xu Tong [a], Yan Li [b,*], M.W. Fu [a,*]

[a] Department of Mechanical Engineering, Research Institute for Advanced Manufacturing, The Hong Kong Polytechnic University, Hong Kong, China
[b] Thayer School of Engineering, Dartmouth College, Hanover, NH 03755, USA

ARTICLE INFO

Keywords:
Microforming
Crystal plasticity
Grain size effect
Progressive microforming
CPFEM-CZM
Product quality control

ABSTRACT

Progressive microforming is widely recognized as one of the most efficient and desirable methods of mass production in micromanufacturing arena. To predict the deformation behaviour and size effects of materials induced in progressive microforming, the finite element method (FEM) employed for modelling the microforming process needs to account for microstructure details and deformation/failure mechanisms of the materials. This led to the development of the novel crystal plasticity finite element method (CPFEM) and cohesive zone model (CZM). Previous research and application of CPFEM have been mainly limited to simple deformations such as uniaxial tension and compression, whereas the new method can provide physical insights into how the grain size affects the interplay between crystallographic slip and mechanical twinning in complex microforming, and further material deformation during sheet blanking. A case study was conducted to manufacture a hexagonal socket part using a three-step progressive microforming system, with the comparison between experiments and CPFEM simulations focusing on microstructure evolution, deformation load, and product quality. The CPFEM was found to be more reliable than the conventional FEM in predicting complex deformation, particularly in microstructure and texture evolution, dimensional accuracy and irregular geometries. Results showed that the total height of the part increases with the decreasing grain size, while the head diameter rises with grain size. Simulations successfully anticipated the distributions of dead metal zones and shear bands and identified hole and rollover geometries and corresponding grain size effects. In conclusion, this research facilitates the understanding of grain size effects on the deformation behaviour in progressive microforming and presents a novel approach and strategy for modelling, prediction, and product quality assurance in complex micro deformation and forming processes.

1. Introduction

Microforming, a deformation-based micro-scaled manufacturing technique, has emerged as a highly sophisticated and indispensable technology for making different micro parts and structures, such as microelectronics, aerospace, and biomedicine, in conjunction with meeting the ever-evolving demands of human life [1–3]. Among the various manufacturing methods, progressive microforming has emerged as one of the most sought-after techniques for mass production [4,5]. Progressive microforming, as the term suggests, involves a series of sequential forming steps to produce micro-scaled components with intricate shapes directly from metal sheets [6,7]. This method offers several notable advantages. Firstly, it overcomes challenges related to the positioning, transportation, and ejection of both the sheet metal and the preform [8,9]. Additionally, it streamlines tooling design by executing multiple operations simultaneously, resulting in enhanced efficiency and significant time savings [10,11].

Despite its benefits, fabricated components often exhibit significant scattering in product quality and feature dimensions when the ratio of initial grain size (d) to sheet thickness varies, as observed in the field of microforming [12–14]. These size effects (SEs) significantly affect manufacturing reliability and quality control in terms of loading condition, dimensional accuracy, geometry irregularity, surface quality, etc. [15–17]. To address this issue, researchers developed many progressive forming systems to study the SEs through physical experiments. For instance, Fu and Chan [18,19] developed a three-step progressive forming process to directly create micro- and meso-hollow flanged scaled parts. Their findings indicated that finer-grained materials require a higher forming load and stress, and that material strength is decreased with increasing grain size, in line with the Hall-Petch relation. Zhang et al. [20], on the other hand, developed a multi-stage microembossing system using SS 316 L and found similar SEs while making

* Corresponding authors.
E-mail addresses: yan.li@dartmouth.edu (Y. Li), mmmwfu@polyu.edu.hk (M.W. Fu).

https://doi.org/10.1016/j.ijmecsci.2024.108971
Received 17 June 2023; Received in revised form 16 December 2023; Accepted 1 January 2024
Available online 2 January 2024

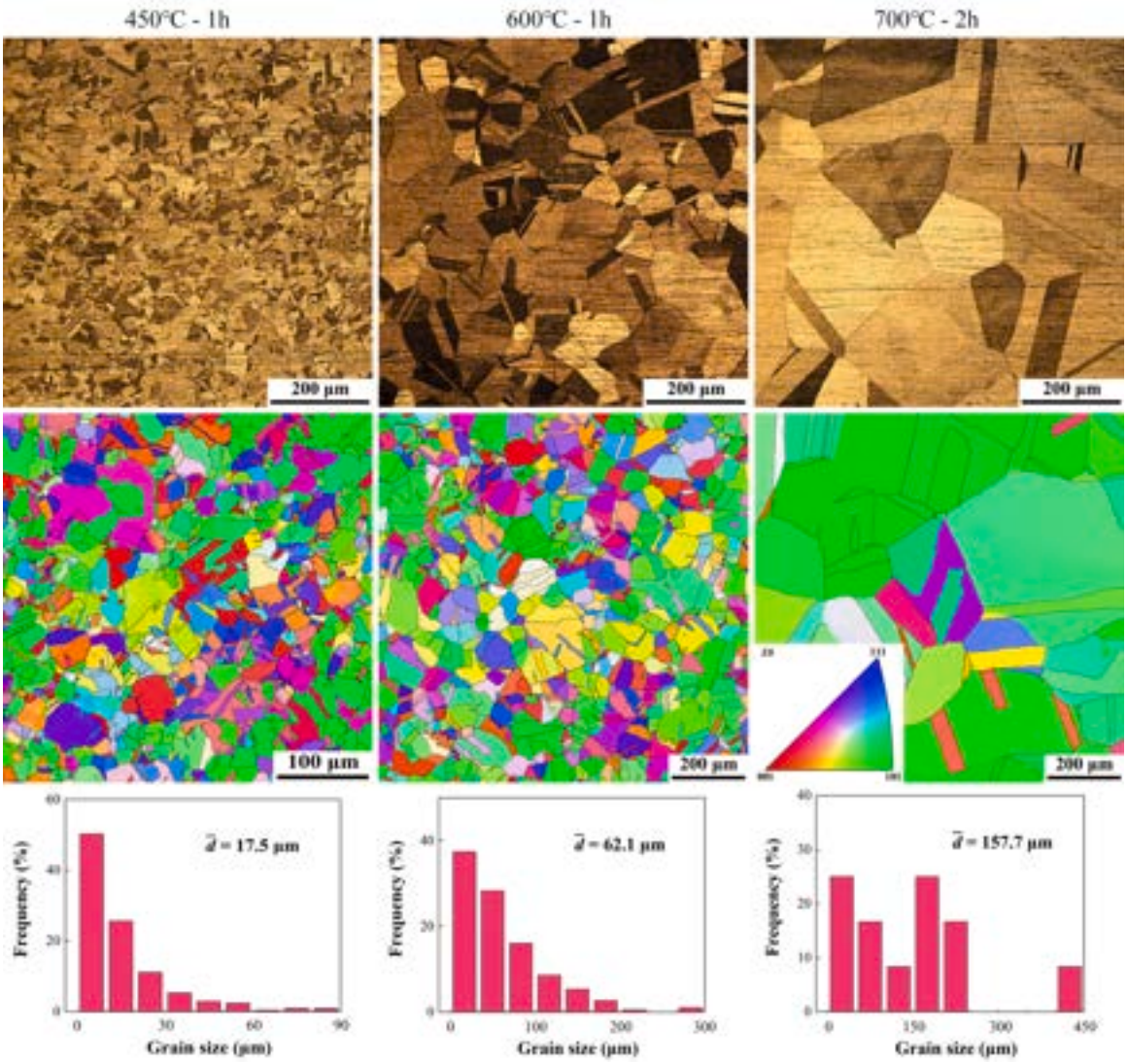

Fig. 1. The metallographic images and EBSD grain orientation mappings of the CuZn32 sheets under heat treatment conditions of 450℃−1 h, 600℃−1 h, and 700℃−2 h. The average grain sizes were calculated from the EBSD results as 17.5 μm, 62.1 μm, and 157.7 μm, respectively.

micro channels with various grain sizes. Furthermore, Meng et al. [21] and Zheng et al. [22] utilized similar four-step progressive microforming systems to make more intricate parts, including double-flanged and conical-flanged components. Their studies investigated the grain SEs and sheet thickness SEs on the dimensional accuracy and geometry irregularity. The results showed a reduction in dimensional accuracy and surface finish with coarser-grained materials. It is worth noting that the grain SEs on manufacturing processes and product quality can vary significantly, depending on the specific component and forming design employed. For instance, the extrusion length in a flat plunger part increases with grain size [23], while the opposite trend has been detected in another progressive formed micropart [24]. Consequently, relying solely on experiments to predict SEs is not a feasible technique due to the high cost of mass production. Despite the presence of simulations in the aforementioned literature, particularly the conventional finite element method (FEM) that utilizes material properties derived from tensile tests, none of these simulations have been able to provide an accurate prediction for grain SEs regarding dimensional accuracy and surface quality. Therefore, in order to accurately predict and mitigate the SEs, it is crucial to establish an efficient simulation framework specifically tailored for complex deformations like progressive microforming. This new framework is indispensable for enhancing the precision of the microforming process and ensuring the high quality of manufactured parts. By enabling accurate and stable prediction and simulation during the initial design phase, the framework supports informed decision-making regarding micro-part and tooling design, process optimization, and quality control.

The crystal plasticity finite element method (CPFEM) has emerged as a promising tool to address the complex issues of material deformation and processing in recent years [25–27]. CPFEM captures important microscale phenomena, such as crystallographic grain orientations, dislocation interactions, and material texture, which are critical for understanding the root causes of property scattering and uncertainties in manufacturing compared to conventional FEM, which assumes isotropy at the macroscale level [28–30]. While earlier studies involving CPFEM focused on investigating deformation mechanism [31,32], in-grain texture evolution [33,34], and hardening and fracture behaviours [35,36] by conducting simple tests, such as tension [37], compression [38], torsion [39], bending [40], its application to understanding deformation behaviours during progressive microforming is limited. This limitation is due to the intricate nature of component shape and the inability to adequately capture critical issues such as significant material flow and microstructure evolution. Although there have been limited attempts to use CPFEM to study SEs in complex deformations, progress has been

Table 1
Chemical composition of the as-received CuZn32 sample.

Content (mass fraction,%)						
Cu	Fe	Sb	Bi	P	Pb	Zn
67.50	0.1	0.005	0.002	0.01	0.03	Bal.

made. Cao et al. [41] employed CPFEM to simulate forward extrusion, while Guo et al. [42] studied the SEs in micro deep drawing via a holistic model of a TWIP sheet and found consistent results with experiments and CPFEM simulations. Adzima et al. [43] investigated the springback behaviour for a micro connector by using two crystal plasticity models, and Zhang et al. [20] conducted multi-stage sheet microforming simulations. Tong et al. [44] validated the results of the CPFEM in a micro-embossing process of a multi-channel structure and observed the same grain SEs in product dimensions and surface quality as in experimental results. These studies indicate that CPFEM can effectively demonstrate microstructural evolution and SEs in complex deformations, providing a basis for further application of this method to the field of progressive microforming.

In progressive microforming processes using sheet metals, fractures become inevitable due to the substantial strains involved [45,46]. To date, most CPFEM work has used element deletion as a method for crack modelling [47,48]. This approach, however, is prone to numerical instability or mesh distortion when a large number of elements are deleted in progressive forming. The cohesive zone model (CZM), which involves embedding cohesive surfaces along bulk element boundaries as part of the physical model, offers a better solution [49,50]. A computational model that integrates CPFEM and CZM offers several advantages and can effectively address the deformation and failure mechanisms that may not be adequately captured by other approaches. By specifying constitutive relations for the bulk phases and cohesive surfaces separately, CPFEM can provide important insights into the effect of grain size on material properties and deformation mechanisms, while CZM can explicitly resolve deformation-induced failure mechanisms, thus providing proactive process design guidelines that can reduce the risk of undesirable failures or defects. In 1993, the combination of CPFEM and CZM was first proposed by Xu and Needleman [51] for the research of fracture behaviour in metal matrix material, where the CZM was applied to model the interface between matrix and inclusions. Ten years later, Clayton and McDowell [52,53] conducted a series of studies on CPFEM-CZM for polycrystalline materials, in which CZM was used for failure simulation in grain boundaries. Zhao et al. [54], Ghodrati et al. [55], and Yalçinkaya et al. [56] subsequently applied this technique to analyze intergranular fracture in creep-fatigue, rolling-fatigue, and tension deformation, respectively. For most metallic materials, intergranular fracture and transgranular fracture occur simultaneously. Therefore, Lyu et al. [57] proposed a hierarchical higher-order multi-scale CZM to simulate fracture and crack propagation in crystalline solids. They found that the transition from intergranular fracture to transgranular fracture was sensitive to both the grain size and grain strength.

This study proposes a novel CPFEM approach aimed at investigating and understanding the impact of grain SEs on uncertainties in product quality and feature dimensions in progressive microforming. This paper is structured as follows: First, a progressive microforming system that directly utilizes the CuZn32 sheet is developed, and the prepration of the materials and uniaxial tensile test are described in Section 2. Next, Section 3 introduces the CPFEM and CZM method, parameter determination, and modelling details. In Section 4, the grain SEs on true stress, forming load, dimensional accuracy, undesirable geometry, and surface quality are analyzed. Finally, the main conclusions of this study are summarized in Section 5.

2. Experimental methodology

The experimental procedure involved preparing the testing material, conducting uniaxial tensile tests and progressive microforming were introduced. To investigate grain SEs, heat treatments and microstructure observations, including microscopy and EBSD, were performed. Macroscope uniaxial tensile tests were then conducted to obtain the mechanical responses of the prepared material with various grain sizes. Finally, a progressive microforming system was developed to fabricate a hexagonal socket part.

2.1. Testing materials and uniaxial tensile test

To thoroughly investigate the grain SEs, the brass sheet material with a thickness of 1000 μm was subjected to a range of heat treatments with varying conditions, including 450℃−1 h, 600℃−1 h, and 700℃−2 h. Microstructural observations were made through both optical microscopy and electron backscatter diffraction (EBSD), as depicted in Fig. 1. The composition of the brass CuZn32 sheet is shown in Table 1. The samples were cut, polished, and then etched for 8–10 s, while those intended for EBSD examination underwent electrolytic polishing. The acquisition and analysis of images were executed using the HKL 5-channel software package in conjunction with the EBSD system, with step size parameters of 1 μm and 2.5 μm, respectively. Data from the EBSD tests were utilized in the crystal plasticity model as described in Section 3.1, enabling a more accurate determination of average grain sizes for modelling and constitutive model calibration purposes. In this study, CuZn32 sheets with varying average grain sizes of 17.5 μm (fine grain - FG), 62.1 μm (medium grain - MG), and 157.7 μm (coarse grain - CG) were utilized in both uniaxial tensile tests and the progressive microforming process. The pole figures of the sheets for various grain sizes with a reference direction norm to the RD-ND section are illustrated in Fig. 2(a).

Quasi-static uniaxial tensile tests were conducted along RD using a programmable MTS testing machine and an extensometer, and sample dimensions are illustrated in Fig. 2(b). The tests were performed at a strain rate of 0.001 s^{-1} at room temperature to determine the correlation between grain size and the mechanical response of the specimens. The engineering stress and strain data can be directly obtained from the software linked with the MTS and extensometer, which would be transferred to true stress and strain data. The test setup and sample configurations followed ASTM: E8/E8M standards and three samples were prepared for each grain size. The average true stress-strain response of the three samples was used to represent their macroscopic constitutive relationships. The goal of these experiments was to provide material information that could be integrated into both the conventional FEM framework and the CPFEM framework.

2.2. Progressive microforming process

Through progressive microforming, the study fabricated a hexagonal socket part as shown in Fig. 3(c). Such socket parts with similar geometric configurations are typically produced using turning or extrusion processes. However, progressive forming has high efficiency and capacity to produce high-quality products. The tooling system utilized in the study, as illustrated in Fig. 3**(a)**, consists of a platform, a blank holder, a die holder, a bottom plate, and three sets of punch and die, all made of Cr12 cold-work die steel. During the microforming process, an 80 mm × 20 mm × 1 mm brass sheet was fed through the system from left to right. processing by 20 mm per step. Following two forward extrusion steps and a blanking step, the final product was deposited onto the bottom plate. Step I of the microforming process employed a punch with a 1 mm radius to effect a 0.6 mm movement along the thickness direction. The material was extruded into a 0.5 mm radius tunnel with a 0.2 mm-45° chamfer. If a columnar material is employed, the extrusion ratio at this stage would reach 2. In Step II, a hexagon socket with 0.25

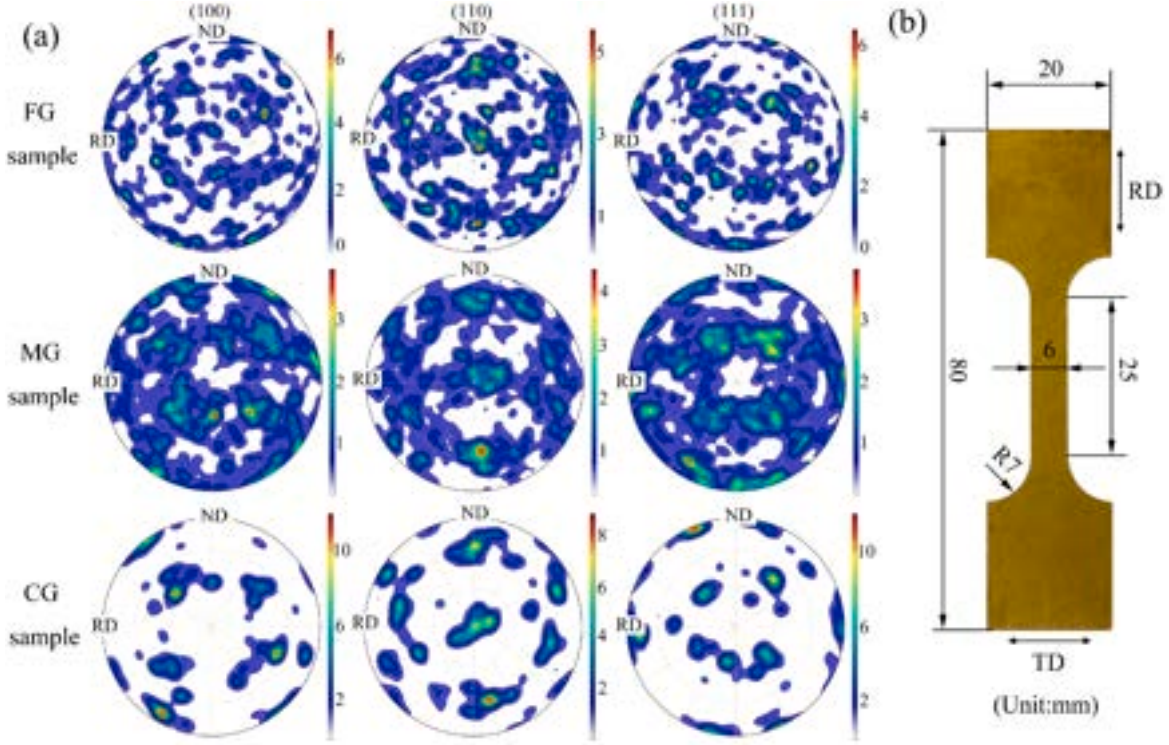

Fig. 2. (a) Pole figures of CuZn32 for different initial grain sizes with a reference direction norm to RD-ND section and (b) specimen design for the uniaxial tensile tests.

mm thickness and 0.8 mm diagonal distance was formed via forward extrusion at the top of the material. Finally, in Step III, a punch with a 0.8 mm radius was used to completely cut the part. A uniform slow punch speed of 0.005 mm/s was employed to eliminate the impact of strain rate in all three steps. Mechanical oil was used as a lubricant on each interface to reduce friction. The resulting microparts are shown in Fig. 3**(d)**.

3. Constitutive relations and modelling details

This section introduces a novel CPFEM and CZM method, which incorporates the effects of slip and twinning on deformation behaviour in brass materials in the CPFEM part, while the CZM considers the separation of material. CPFEM parameters were then determined and validated through the simulations of uniaxial tensile tests. Finally, the modelling of progressive microforming was introduced using this method.

3.1. Crystal plasticity constitutive model

The total deformation gradient $\boldsymbol{F}$, imparted upon a crystalline material by means of crystal slip and twinning, can be decomposed into two constituent parts: the plastic deformation gradient $\boldsymbol{F}^p$ (from slip and deformation twinning) and the elastic deformation gradient $\boldsymbol{F}^e$ (from the reversible stretching and rotation of the crystal lattice):

$$\boldsymbol{F} = \boldsymbol{F}^e \cdot \boldsymbol{F}^p = \boldsymbol{F}^e \cdot \boldsymbol{F}^{twin} \cdot \boldsymbol{F}^{slip}. \tag{1}$$

The velocity gradient tensor $\boldsymbol{L}$ can be composed of the elastic deformation velocity gradient tensor $\boldsymbol{L}^e$ and the plastic deformation velocity gradient tensor $\boldsymbol{L}^p$ as:

$$\boldsymbol{L} = \dot{\boldsymbol{F}} \cdot \boldsymbol{F}^{-1} = \dot{\boldsymbol{F}}^e \cdot \boldsymbol{F}^{e\,-1} + \boldsymbol{F}^e \cdot \dot{\boldsymbol{F}}^p \cdot \boldsymbol{F}^{p\,-1} \cdot \boldsymbol{F}^{e\,-1} = \boldsymbol{L}^e + \boldsymbol{L}^p, \tag{2}$$

$$\boldsymbol{L}^p = (1 - f^{tw}) \sum_{\alpha}^{N^s} \dot{\gamma}^{\alpha} (\boldsymbol{m}^{\alpha} \otimes \boldsymbol{n}^{\alpha}) + \sum_{\beta}^{N^{tw}} \dot{\gamma}^{\beta} (\boldsymbol{m}^{\beta} \otimes \boldsymbol{n}^{\beta}). \tag{3}$$

Here $\boldsymbol{L}^p$ is contributed by 12 {111} ⟨110⟩ slip systems and 12 {111} ⟨112⟩ twinning systems [58]. $\dot{\gamma}^{\alpha}$ and $\dot{\gamma}^{\beta}$ denote the shearing rate on the α^{th} slip system and β^{th} twinning system. $f^{tw} = \sum f^{\beta}$ is the volume fraction of all twinning systems, which can be calculated by $f^{tw} = \sum f^{\beta} = \sum \gamma^{\beta} / \gamma^{tw}$. In this equation, γ^{β} is the calculated shear strain in the β^{th}twinning system, and γ^{tw} is the reference total twinning shear strain. In FCC materials, $\gamma^{tw} = 0.707$ [59]. N^s and N^{tw} are the numbers of slip and twinning systems, taking the value of 12. $\boldsymbol{m} \otimes \boldsymbol{n}$ is the Schmid factor.

According to the assumption of Kalidindi [58], only the effects between twinning and slip systems were considered in the working hardening model. The internal effects between different slip systems and twin systems were neglected. The following equations were used for the description of the shear rate:

$$\dot{\gamma}^{\alpha} = \dot{\gamma}_0^{\alpha} \left| \frac{\tau^{\alpha}}{g^{\alpha}} \right|^{1/m} sign(\tau^{\alpha}), \tag{4}$$

$$\dot{\gamma}^{\beta} = \begin{cases} \dot{\gamma}_0^{\beta} \left| \dfrac{\tau^{\beta}}{g^{\beta}} \right|^{1/m} & f^{tw} < 0.8, \\ 0 f^{tw} = 0.8 \ or \ \tau^{\beta} \le 0. \end{cases} \tag{5}$$

Here, γ_0^{α} and γ_0^{β} are reference strain rates of slip and twinning. τ^{α} and τ^{β} are the corresponding resolved shear stresses. g^{α} and g^{β} are the critical resolved shear stress (CRSS) to resist slip and twinning evolution. m is the rate-sensitivity factor. The upper limit on the total volume fraction of twins is selected as 0.8 [58]. The evolution of g^{α} and g^{β} can be formulated as:

$$g^{\alpha} = h_s^{\alpha} \left(1 - \frac{g^{\alpha}}{g_s^{\alpha}} \right) \sum \gamma^{\alpha}, \tag{6}$$

$$h_s^{\alpha} = h_s \left[1 + a (f^{tw})^b \right], \tag{7}$$

$$g_s^{\alpha} = g_0 + g_{pr} (f^{tw})^{0.5}, \tag{8}$$

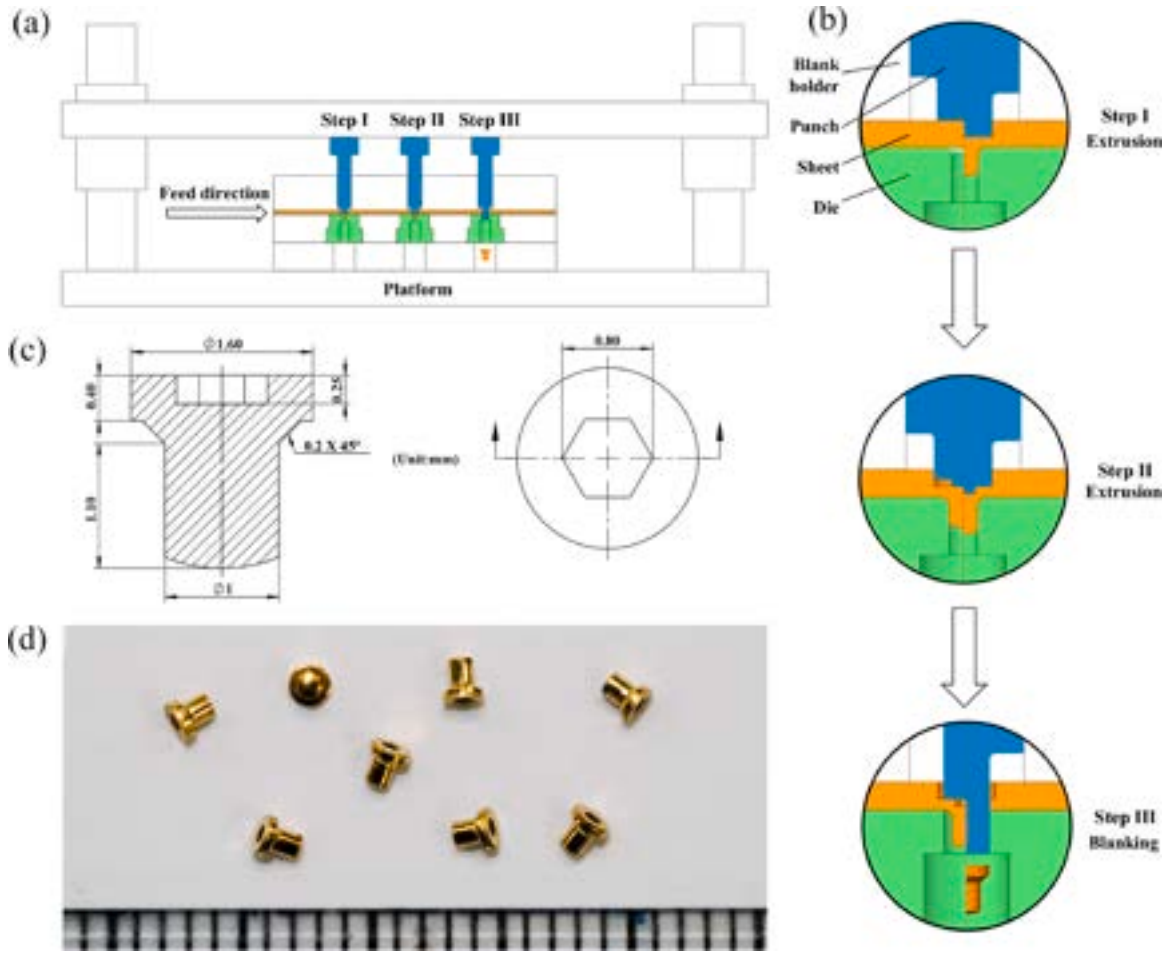

Fig. 3. The developed progressive microforming setup and the designed and fabricated hexagonal socket part. (a) The progressive microforming system consists of an outer platform, blank and die holders, and three sets of punches and dies. (b) Schematic diagram of the processing in the three steps, including two extrusions and one blanking. (c) The design dimensions of the hexagonal socket part. (d) The final fabricated hexagonal socket part made by CuZn32.

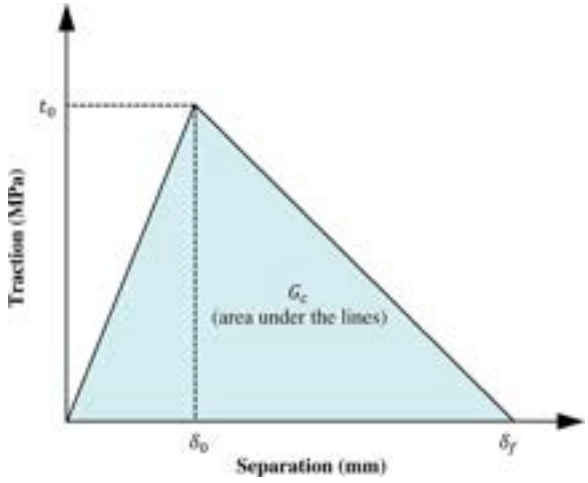

Fig. 4. Typical bi-linear traction-separation response used in CZM, involving two stages: the elastic deformation stage and the damage stage. The critical damage energy indicating the complete failure of the cohesive element could be identified as the area under the curve.

$$g^{\beta} = \eta g^{\alpha}. \tag{9}$$

Here, h_s^{α} is the hardening rate and g_s^{α} is the saturated slip resistance. Following the work of Salem et al. [60] and Kalidindi [61], the effects of twinning on slip can be characterized as the effects of the total volume fraction of twinning systems on h_s^{α} and g_s^{α} of the α^{th} slip system. *a, b*, and η are material constants. g_0 is the saturated slip resistance in the absence of twinning and g_{pr} describes the contribution of the Hall–Petch effect.

3.2. Cohesive zone model

The constitutive relations governing the behaviour of the CZM in finite element analysis are described through the utilization of a Traction Separation Law (TSL). The TSL posits a dependence of the traction force on both the normal and tangential displacements. Characterization of the CZM requires consideration of three fundamental features: material stiffness, damage initiation criterion, and damage evolution law [62]. The bi-linear TSL depicted in Fig. 4 encompasses both the elastic and damage stages. Initially, traction strength linearly builds up as separation increases. Once it reaches the peak t_0, damages start to occur. Further separation promotes damage accumulation due to material softening. A complete material fracture occurs once the separation strength reduces to zero. The corresponding critical separation is δ_f. In this study, the maximum nominal stress criterion (MAXS) was chosen as the damage initiation criterion according to:

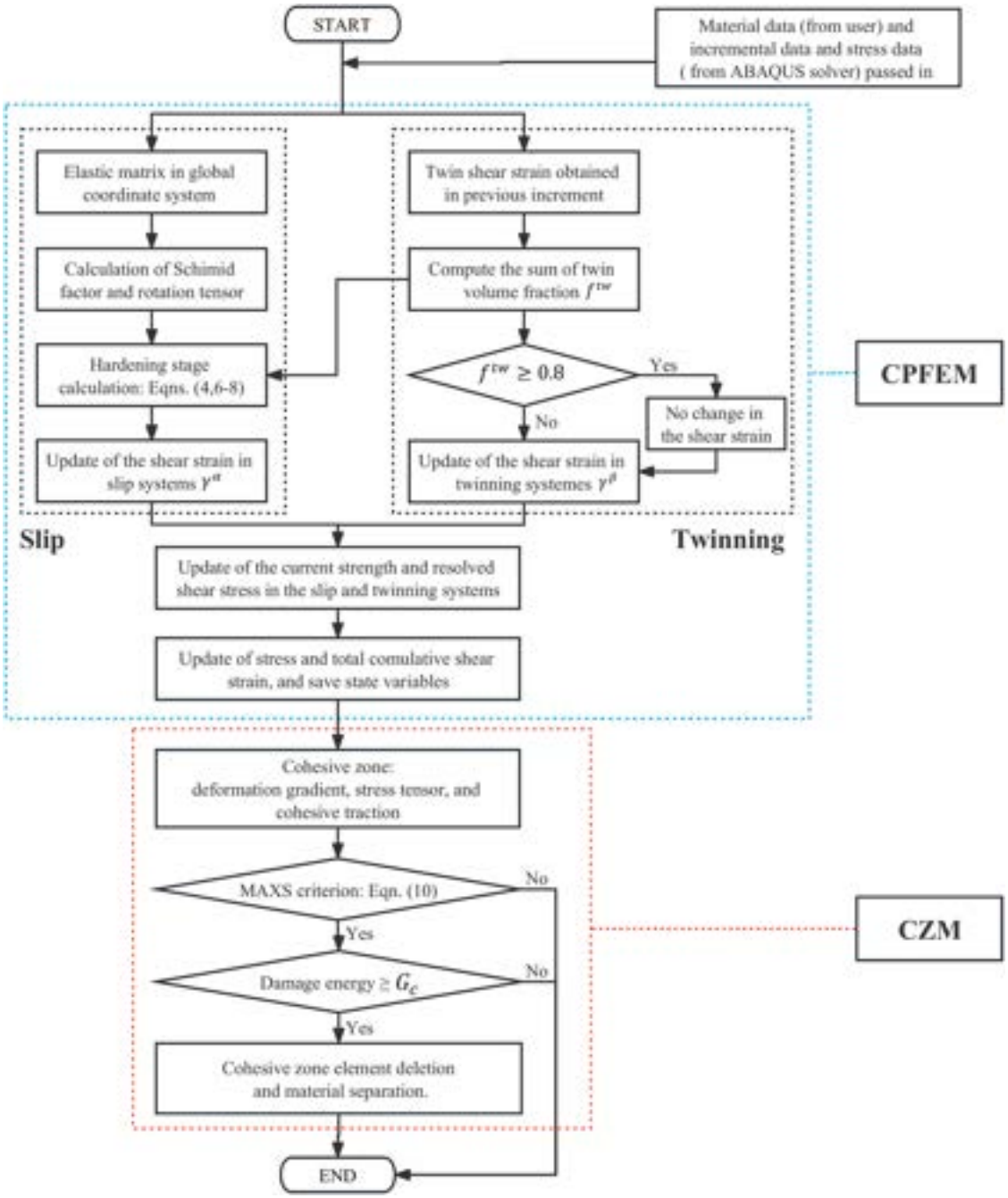

Fig. 5. The algorithm flow chart of the CPFEM and CZM method. The first stage represents the CPFEM part, involving the updates of stress and strain for various slip and twinning systems. The results are passed to the CZM stage to calculate the mechanical behaviour of the cohesive element and determine whether it would fail.

Table 2
Elastic constants and hardening parameters of CuZn32 used in the CPFEM.

C_{11} (GPa)	C_{12} (GPa)	C_{44} (GPa)	$\dot{\gamma}_0^{\alpha}$ (s^{-1})	$\dot{\gamma}_0^{\beta}$ (s^{-1})	m
145	110	70	0.001	0.001	0.02
g_0^{β} (MPa)	g_{pr} (MPa)	α	b	η	
60	350	5	10	1.25	
d (μm)	g_0^{α} (MPa)	g_0 (MPa)	h_s (MPa)		
17.5	60	400	200		
62.1	36	375	190		
157.7	26	360	175		

$$max\left\{\frac{t^n}{t_0^n}, \frac{t^s}{t_0^s}, \frac{t^t}{t_0^t}\right\} = 1. \tag{10}$$

Here t_0^n, t_0^s, and t_0^t are the maximum stresses in the normal direction, the first shear direction, and the second shear direction, respectively. The energy-based damage evolution law was used by defining the damage energy G_c.

3.3. Numerical implementation and model calibration

The flowchart illustrating the sequence of algorithms employed in the new method within one single time step is presented in Fig. 5. The procedure starts with the calculation of the crystal plasticity component, including slip and twinning. This calculation serves as a basis for

Table 3
Parameters used in CZM for various grain sizes.

G_C^n (MPa · mm)	G_C^s (MPa · mm)	G_C^t (MPa · mm)	
51	138	138	
d (μm)	t_0^n (MPa)	t_0^s (MPa)	t_0^t (MPa)
17.5	741	277	277
62.1	621	232	232
157.7	513	191	191

determining whether partial or complete fracture occurs during the deformation process. The whole algorithm was written in a VUMAT subroutine used for the Abaqus/Explicit environment.

For the CPFEM parameters, the elastic parameters were obtained based on the work of Jia et al. [63] and Chiarodo et al. [64]. Kalilindi [61] provided the reference values of γ_0^α, γ_0^β, g_0^β (the initial twinning resistance), a, and b in Eqs. (4)–(7). The initial slip resistance g_0^α was calculated based on Li et al. [65]:

$$g_0^\alpha = \frac{1}{M}\left(\sigma_y + \frac{K}{\sqrt{d}}\right). \tag{11}$$

Here, the Taylor factor $M = 3.06$, and yield stress $\sigma_y = 111$, 72, 55MPa when the average grain size is 17.5, 62.1, and 157.7 μm, respectively. $K = 304\text{MPa} \cdot \mu\text{m}^{1/2}$ represents the Hall-Petch coefficient. Other constitutive parameters were calibrated based on the residuals of the computed values and tensile test results. All parameters used for the CPFEM in this research are listed in Table 2.

Key parameters t_0^n and G_C^n in CZM were determined based on the research of Wang et al. [66] and Cai et al. [59]:

$$t_0^n = 1.35\sigma_f, \text{ and} \tag{12}$$

$$G_C^n = \frac{K_c^2(1-\nu^2)}{E}. \tag{13}$$

Here, σ_f, K_c, ν, and E are the fracture stress, stress intensity factor, Poisson's ratio and Young's modulus. The Poisson's ratio $\nu = 0.34$, and Young's modulus $E = 110\text{GPa}$ [67], and Kumar and Misra [68] gave the

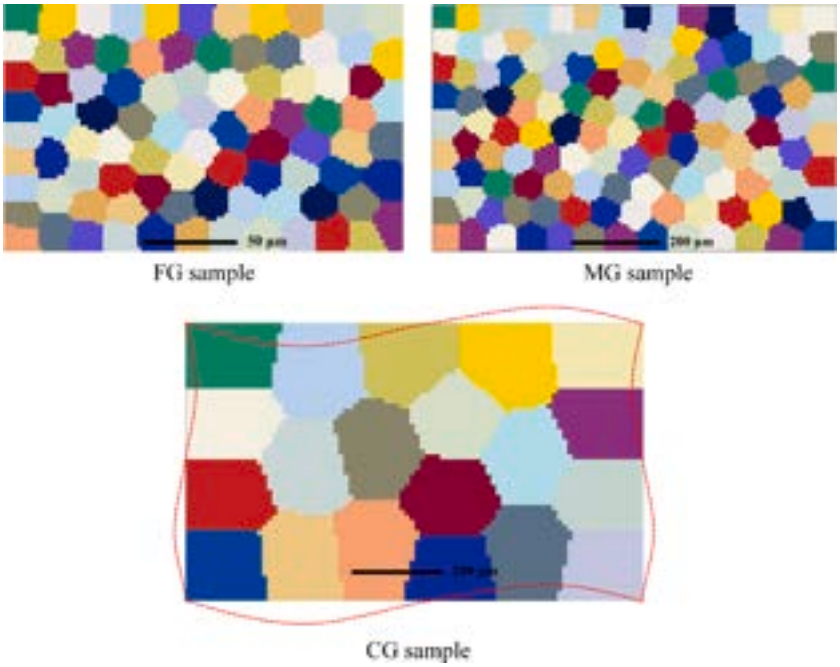

Fig. 6. Illustration of RVEs for various grain sizes and applied periodic boundary conditions. The RVEs were built to show the same surface as the EBSD samples with a reference direction norm to the RD-ND section. The RVE and periodic boundary condition method can reduce the computational cost without compromising the accuracy.

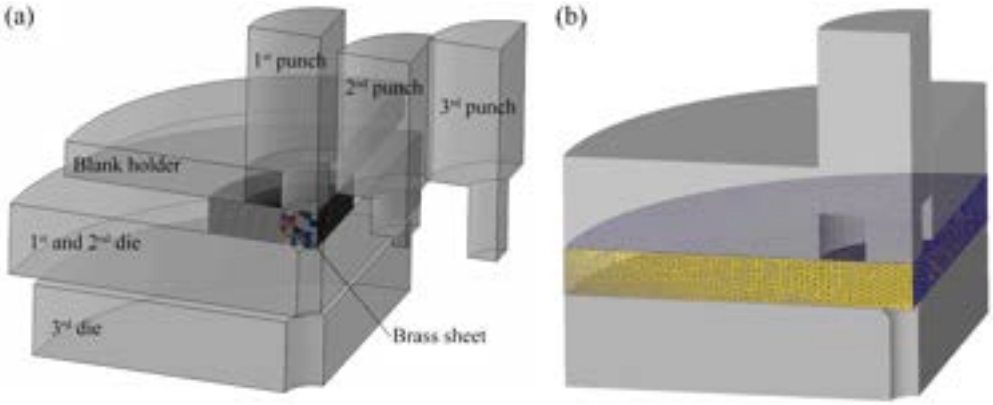

Fig. 7. Modelling of the progressive microforming process using (a) CPFEM and (b) conventional FEM. The simulations were conducted step by step.

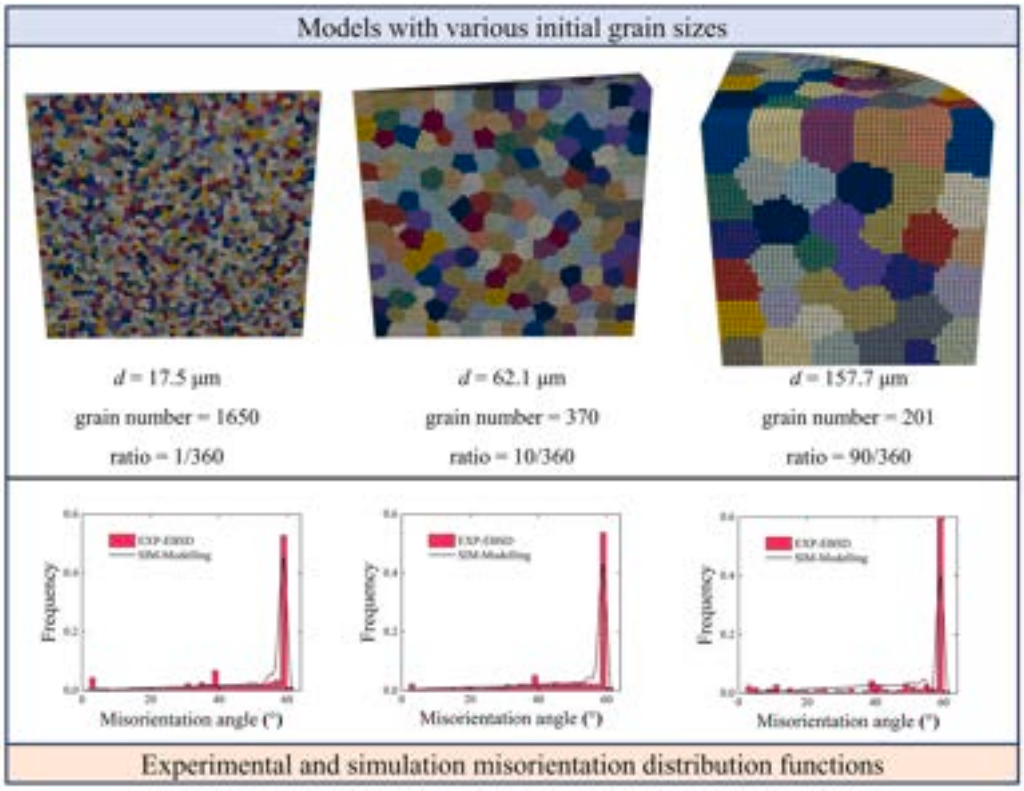

Fig. 8. Models for the progressive microforming CPFEM simulation with information of average gran sizes, grain number involved, and simplification ratio and experimental and simulation misorientation distribution functions (MODFs) in the models. The consistency of the MODFs in the EBSD and the simulation modelling information demonstrates the feasibility of this modelling approach and the reliability of the subsequent simulation results.

specific stress intensity factor of CuZn32 as $K_c = 80\text{MPa} \cdot \text{m}^{-1}$. The damage shear stresses can be calculated via $t_0^s = t_0^t = t_0 /2(1 + \upsilon)$. All parameters used for the CZM in this research are listed in Table 3.

3.4. Modelling of uniaxial tensile test

The study utilized a series of polycrystalline RVEs and implemented them in uniaxial tension simulations using the commercial software Abaqus. The RVEs were divided into the cell aggregates via the Voronoi tessellation method, as illustrated in Fig. 6. To reduce the computational time, only RVEs of the specimen gauge section used in the uniaxial tensile tests were modelled. Since the initial shapes of the grains were regenerated, the grain orientation mapping of the corresponding grains was used in this research. In such a way, the relative positions of the grains corresponding to the grain orientations were fixed, i.e. the grain orientations of the neighbouring grains were determined according to the actual textures to ensure their compatibility. This dimensional manipulation improved the computation efficiency and ensured enough grains were deformed. Furthermore, the grain sizes were averaged as the same as the mean sizes of corresponding samples. Four simulations were conducted for each grain size, considering actual textures from the EBSD results (as shown in Fig. 2**(a)**) and three sets of random textures for comparison. The RVEs were modelled with C3D8 bulk elements, and the periodic boundary conditions were applied to ensure accuracy and reliability.

3.5. Modelling of progressive microforming process

The progressive microforming process was modeled using both CPFEM and conventional FEM. The simulations were performed step by step. As Step I is finished, the 1st punch will move away and the 2nd punch will move to the designated location to start Step II. The conventional FEM simulations were conducted in Deform-3D software. Considering the computational efficiency, only a quarter of the deformed sheet was simulated under symmetric boundary conditions. As illustrated in Fig. 7**(b)**, conventional FEM does not account for microstructure details of the CuZn32 sheet. Its constitutive relationship is directly obtained from uniaxial tensile testing.

For the CPFEM approach, Abaqus software was utilized as the simulation platform. Resolving microstructure details of the entire sheet requires very fine mesh and is therefore impractical for structural scale analysis due to the high computational cost. Therefore, the sheet was modelled by a combination of different zones and different simplification ratios for various grain sizes. For example, the inner region of the sheet that is in direct contact with the punches and dies has a dimension of 1 mm in both radius and thickness, which was set as the crystal plasticity zone for 201 grains for the CG sample as shown in Fig. 7(a). The detailed models of the inner regions of the brass sheet are illustrated in Fig. 8. The models of the inner regions with the grain size of 17.5, 62.1, and 157.7 μm were simplified into 1/360, 10/360, and 90/360 based on their symmetry planes with 1650, 370, and 201 grains, respectively. CPFEM was applied to the inner region while the rest of the CuZn32 sheet followed the isotropic stress-strain relationship obtained from the uniaxial tensile tests. Constitutive behaviour in this region was defined using the CPFEM in Section 3.1, and the actual texture was assigned to the materials. Like the modelling approach described in Section 3.4, the models were first divided into different grains by using the Voronoi tessellation approach. Since the textures obtained by EBSD were measured in 2D, the surface grains of the RVEs were assigned with the initial grain orientation according to the same mapping method to ensure compatibility; the internal grains were then individually assigned with the grain orientations according to the layering. The experimental and simulation misorientation distribution functions (MODF) are given in Fig. 8. The consistency of the EBSD formation and the simulation

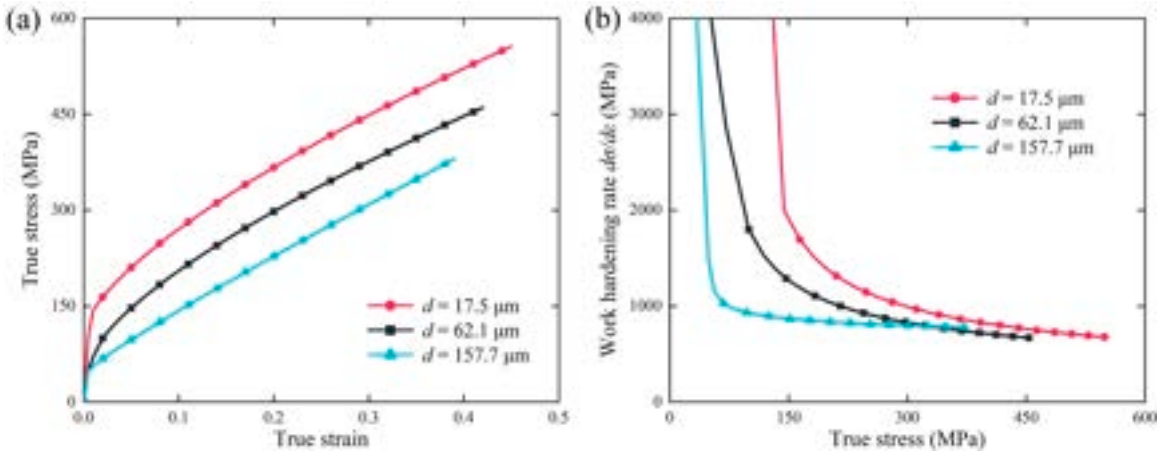

Fig. 9. Comparison of experimental true stress-strain curves and work hardening curves with various grain sizes. These curves show the typical Hall-Petch effect.

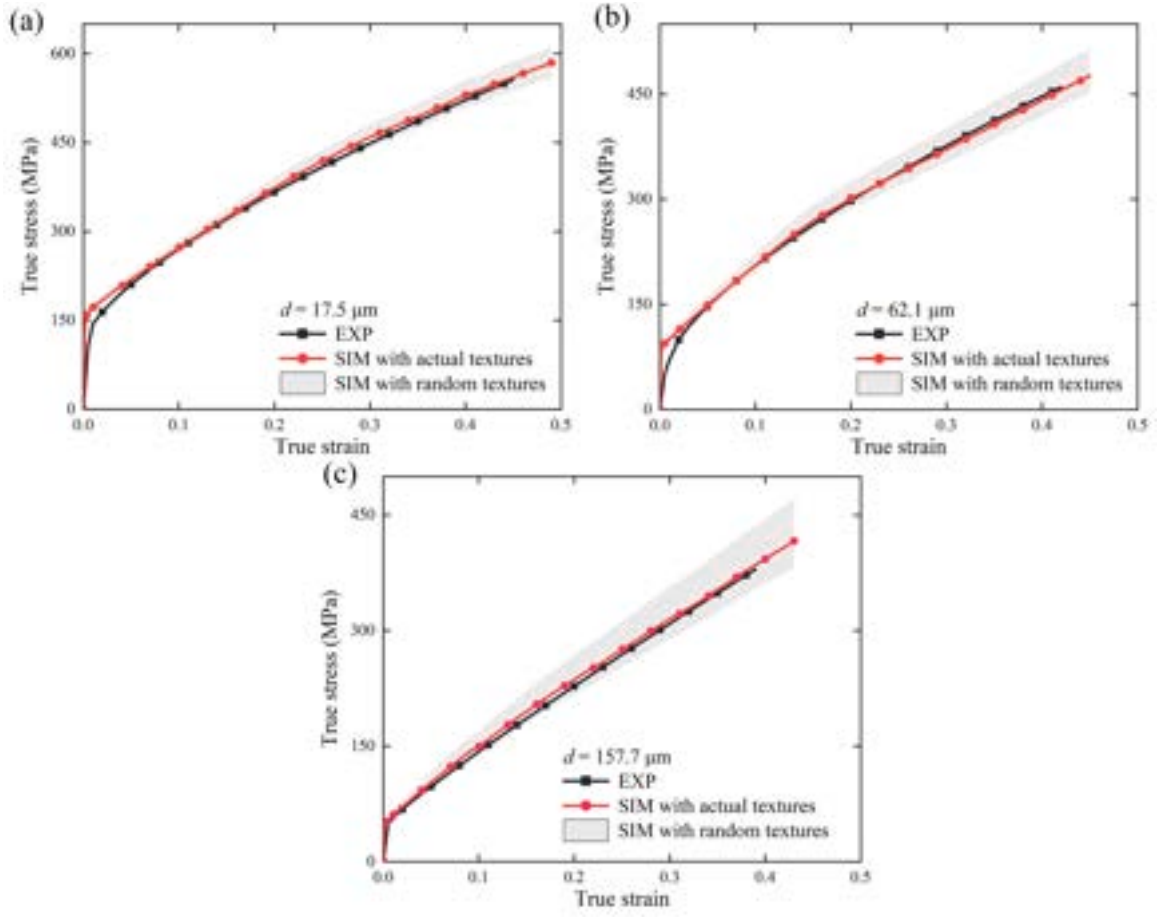

Fig. 10. Comparison of the simulated and experimental true stress-strain curves for (a) FG, (b) MG, and (c) CG samples. The grey areas are obtained by simulations with randomly generated textures. On the one hand, the consistency of the experimental and simulation results validates the CPFEM model and the corresponding parameters; on the other hand, the uncertainty of the results due to the random initial textures proves the necessity of the real texture in the modelling.

modelling information demonstrates the feasibility of this modelling approach and the reliability of the subsequent simulation results.

It is worth noting that in the CPFEM simulation, the distribution of the cohesive elements cannot simply be set as full-field or only on grain boundaries, as the two approaches may result in substantial discrepancies and inaccuracies in simulation results. In this study, cohesive zones were established between elements within the RVEs by considering both intergranular and transgranular fractures. This is because the fracture was only observed within the punch and die contact area during the experiment. Therefore, it is not necessary to embed cohesive elements in other regions where fracture is not likely to occur, as it reduces computational costs without compromising accuracy. C3D8 and COH3D8 were assigned for the bulk elements and cohesive elements, respectively. The shear friction model ($\boldsymbol{f_s = \mu p}$) with a friction coefficient of 0.12 on the lubricated tooling-workpiece interface was employed for both FEM and CPFEM simulations.

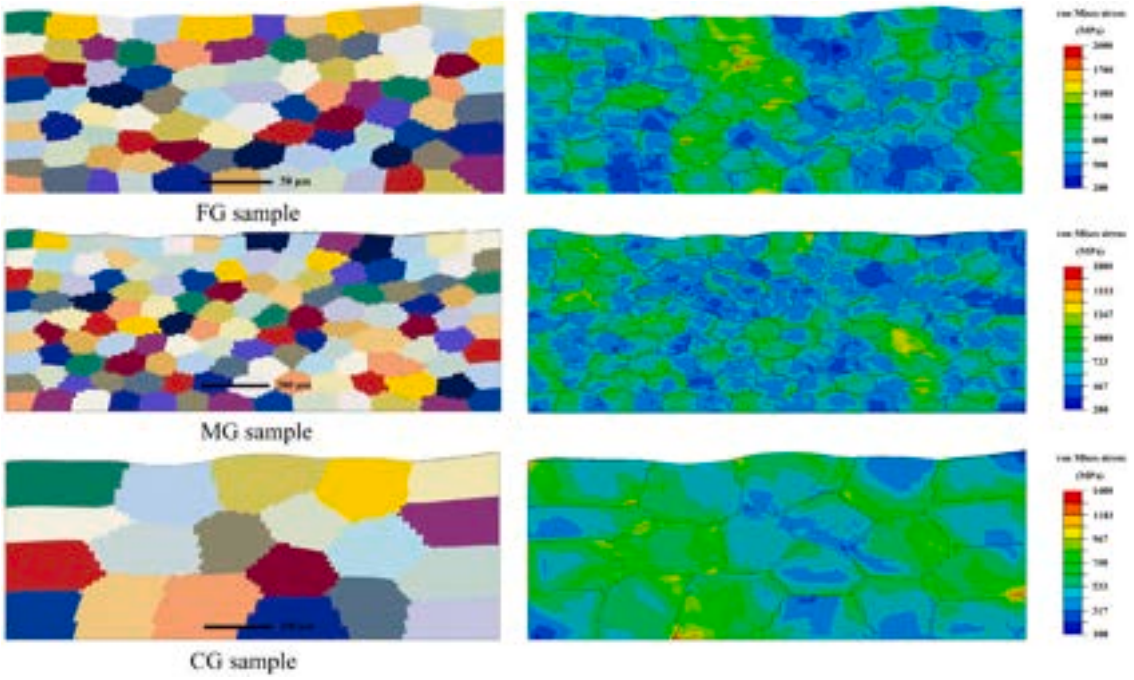

Fig. 11. The deformed results (strain at 0.4) of RVEs under uniaxial tension. The RVEs are modelled with actual textures for FG, MG, and CG samples, respectively. The von Mises stress mappings for each grain size are listed to show the differences.

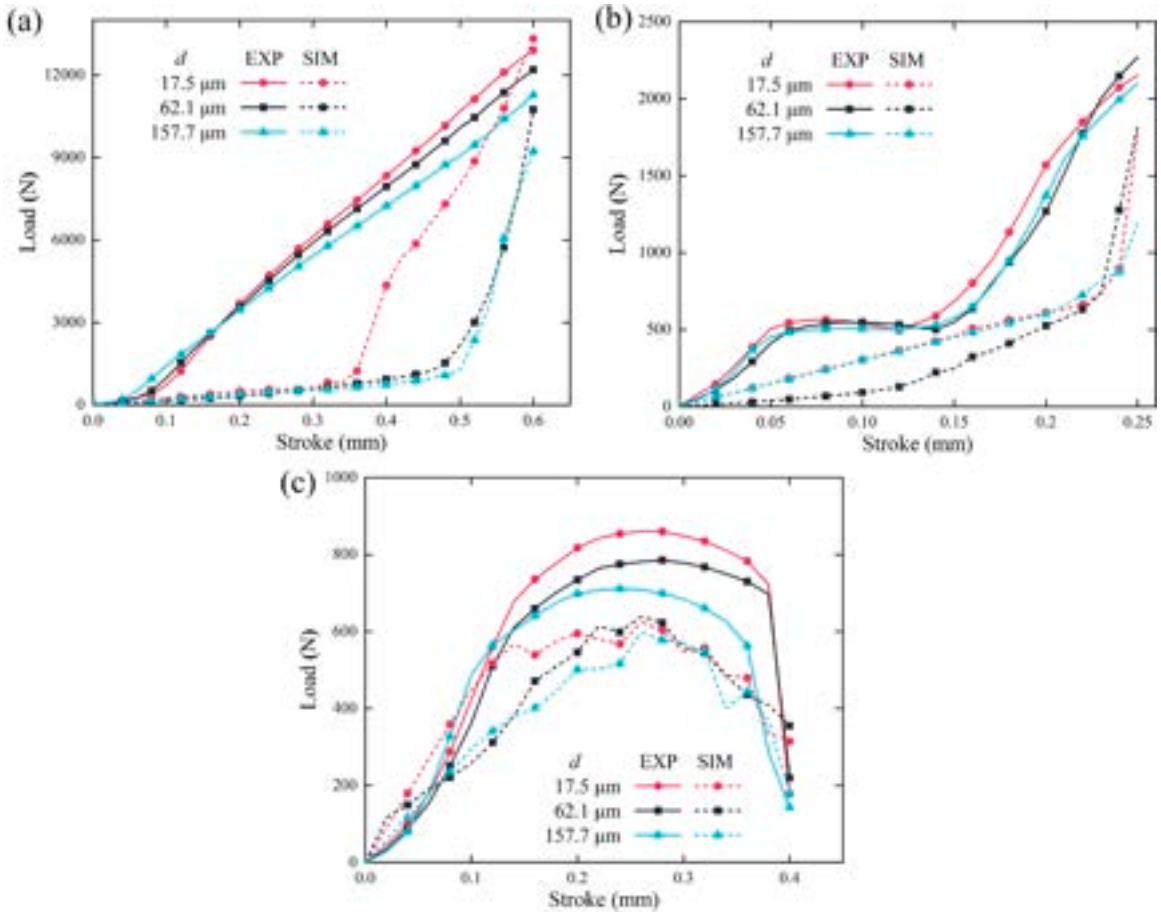

Fig. 12. Comparison of the load-stroke curves between CPFEM simulations and experiments with various grain sizes in (a) Step I, (b) Step II, and (c) Step III.

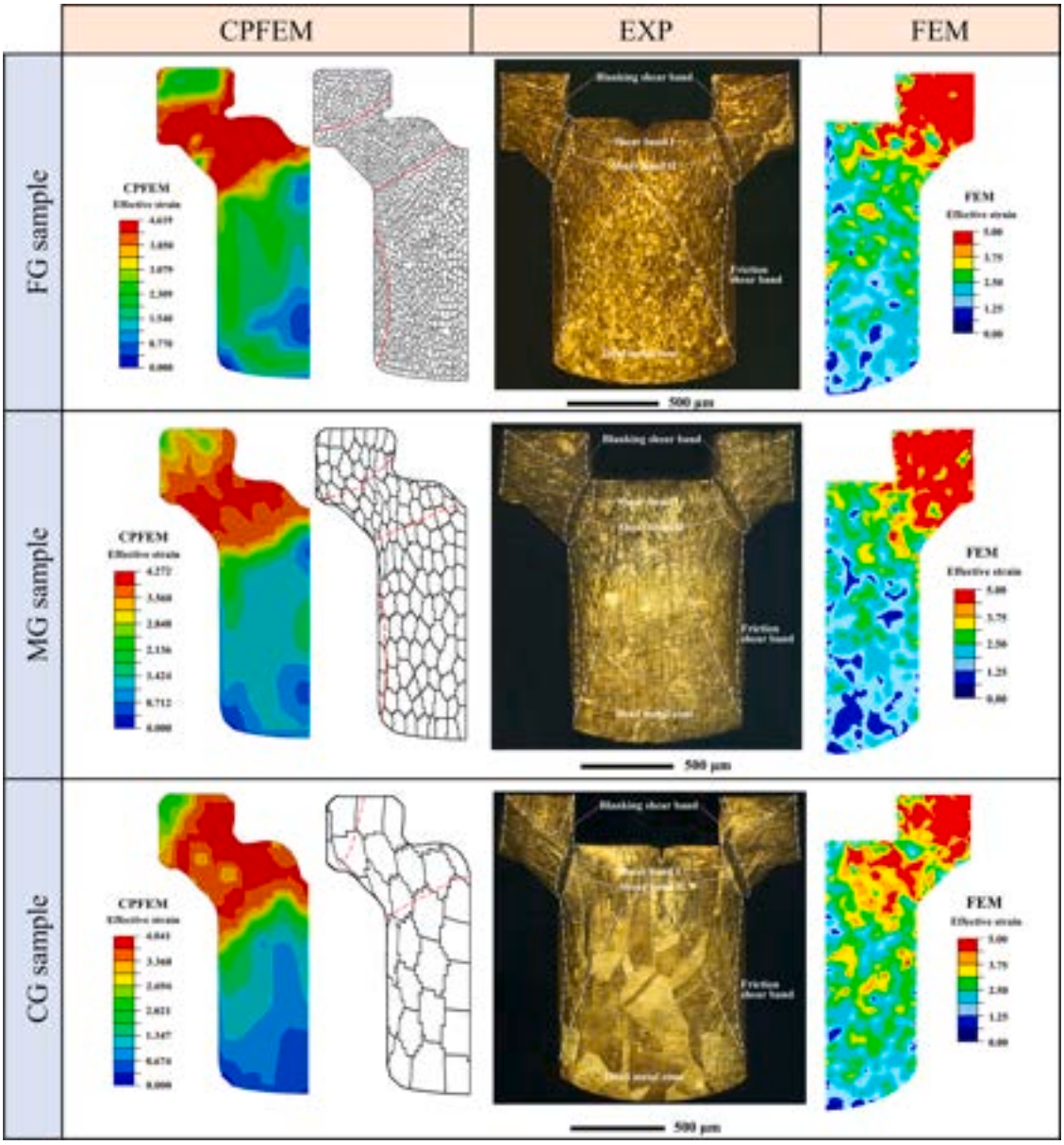

Fig. 13. Comparison of the experimental, CPFEM, and FEM simulated effective strain maps, texture, and microstructure changes of the cross-sections of the formed parts for FG, MG, and CG samples, respectively. The effective strain mapping based on the CPFEM simulation results is calculated using Eq. (14). The metallographic images of the cross-section of the parts indicate the important material flow behaviour and microstructure evolution.

4. Results and discussion

This section analysed the prediction accuracy and feasibility of the newly established CPFEM model by comparing simulated and experimental results in terms of the effects of grain size on the mechanical response of the material, load-stroke relations in progressive microforming, and product quality of fabricated parts. This comparison allowed for an assessment of the effectiveness of the CPFEM in accurately predicting complex deformation and failure behaviour in the progressive microforming process.

4.1. Size effect in tensile test simulation

As depicted in Fig. 9**(a)**, the experimental results indicate that specimens with coarser grain correspond to a lower true stress response and therefore lead to lower initial yield stress due to the reduced grain boundary strengthening effect. Moreover, the coarser-grained specimens were found to be more brittle as the fracture strain decreased with increasing grain size. In CuZn32 microstructure, deformation twinning plays a crucial role, as it is a typical FCC metallic material with low stacking fault energy [69]. In the initial stages of deformation, specimens with finer grains exhibit a higher strain hardening rate due to the severe impediment of dislocation movement at the grain boundaries. This trend does not hold when the truss stress goes beyond a threshold. As indicated in Fig. 9**(b)**, the CG specimen starts to exhibit a higher work hardening rate than the MG one when the true stress is beyond 300 MPa. Deformation twinning generates an additional hardening mechanism. The correlation between work hardening and twinning can be ascribed to three factors: (1) twinning activates the grain splitting, reduces the effective distance of dislocation slip, and facilities strain hardening by the Hall-Petch effect; (2) twinning changes the lattice orientation; and (3) twin region in a less strained matrix is harder than the adjacent non-twin region within a grain according to the Baczynski hardening mechanism [70]. Fig. 10 compares the true stress-strain curves for various grain sizes. A close match between simulation and experiment results was found for samples with real textures. Simulation results for

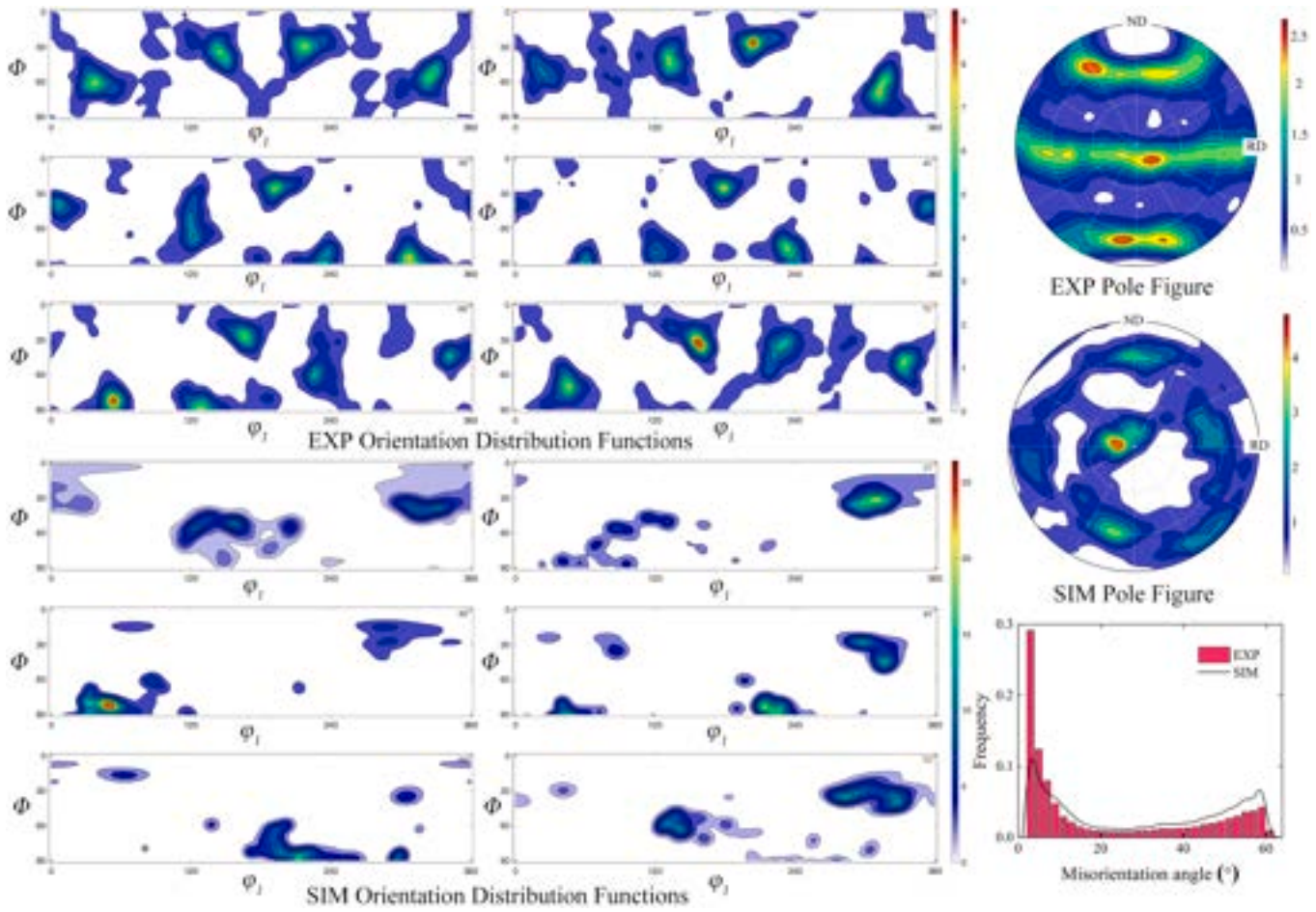

Fig. 14. Comparison of the experimental and CPFEM simulation orientation distribution functions, pole figures, and misorientation distribution functions of the FG sample.

the samples with random textures, which are represented by the shaded areas, tend to exhibit a larger scatter with increasing grain size. This indicates that the CPFEM can provide a good prediction of the strain-hardening behaviour in CuZn32 when the real textures are considered. Therefore, only the actual textures were utilized to model progressive microforming simulation.

The deformed microstructure and the distribution of von Mises stress resulting from the tensile test simulation are depicted in Fig. 11. The analysis revealed several key insights. Firstly, the Hall-Petch relations at the micro-scale hold, as evidenced by the reduction in stress as grain size increases. Upon examination of the experimental results at 0.4 strain (Fig. 9**(a)**), the simulation and experimental results demonstrate a fracture stress ratio of approximately 1.45:1.18:1 and 1.43:1.28:1 for the three different grain sizes, respectively. This close agreement between the simulation and experimental data supports the accuracy of the proposed CPFEM approach and the corresponding parameters. Secondly, certain grains experience significantly greater deformation than others. It is found that grains experiencing higher average stress and strain tend to undergo deformation along the tensile direction and exhibit greater misorientations in relation to the surrounding grains. Lastly, stress concentration occurs more frequently around the grain boundaries of highly deformed grains due to the blocking effect of grain boundaries on dislocation motion and the consequent promotion of twin nucleation and growth in brass materials. The highest stresses are typically concentrated near grain boundaries oriented parallel to the direction of deformation.

4.2. Size effect on load-stroke relation

In this forming process, effective load control not only ensures product quality but also increases the longevity and cost-efficiency of the associated tooling system [71]. Especially, the maximum value of the load will have an impact on the choice of pressure equipment, holding time, and tooling materials in mass production [72,73]. During microforming, correlations between load and stroke in hexagon socket parts with various grain sizes in the three steps are illustrated in Fig. 12 **(a–c)**. In this work, the average results of three sets of repeated experiments were utilized for the load-stroke relations. Since only a part of the material was simulated, the load results of the CPFEM simulation were multiplied by the scale of the model simplification.

It can be observed from Fig. 12(a) that the load in Step I is significantly greater compared to the subsequent two steps, with a difference in maximum value as much as a dozen-fold. During Step I, which involves the first forward extrusion process, the experimental results demonstrate an essentially linear increase in load with a maximum value of approximately 11,000–13,000 N. In contrast, the simulation results show slow growth and then a sharp increase only during the final 0.3 mm or 0.15 mm stage as shown in Fig. 12(a). During Step II, as the forming process continues, the load is initially raised to 500 N and then maintained within this range for strokes ranging from 0.06 to 0.15 mm. Subsequently, the load increases linearly to a range of 2100–2300 N. For the simulation results, a steep increase occurs in the last 0.02 mm stroke, while the maximum load is below 2000 N. Step III necessitates the full extraction of the part from the die tunnel, resulting in a much greater stroke compared to the first two steps according to Fig. 3(b). During Step

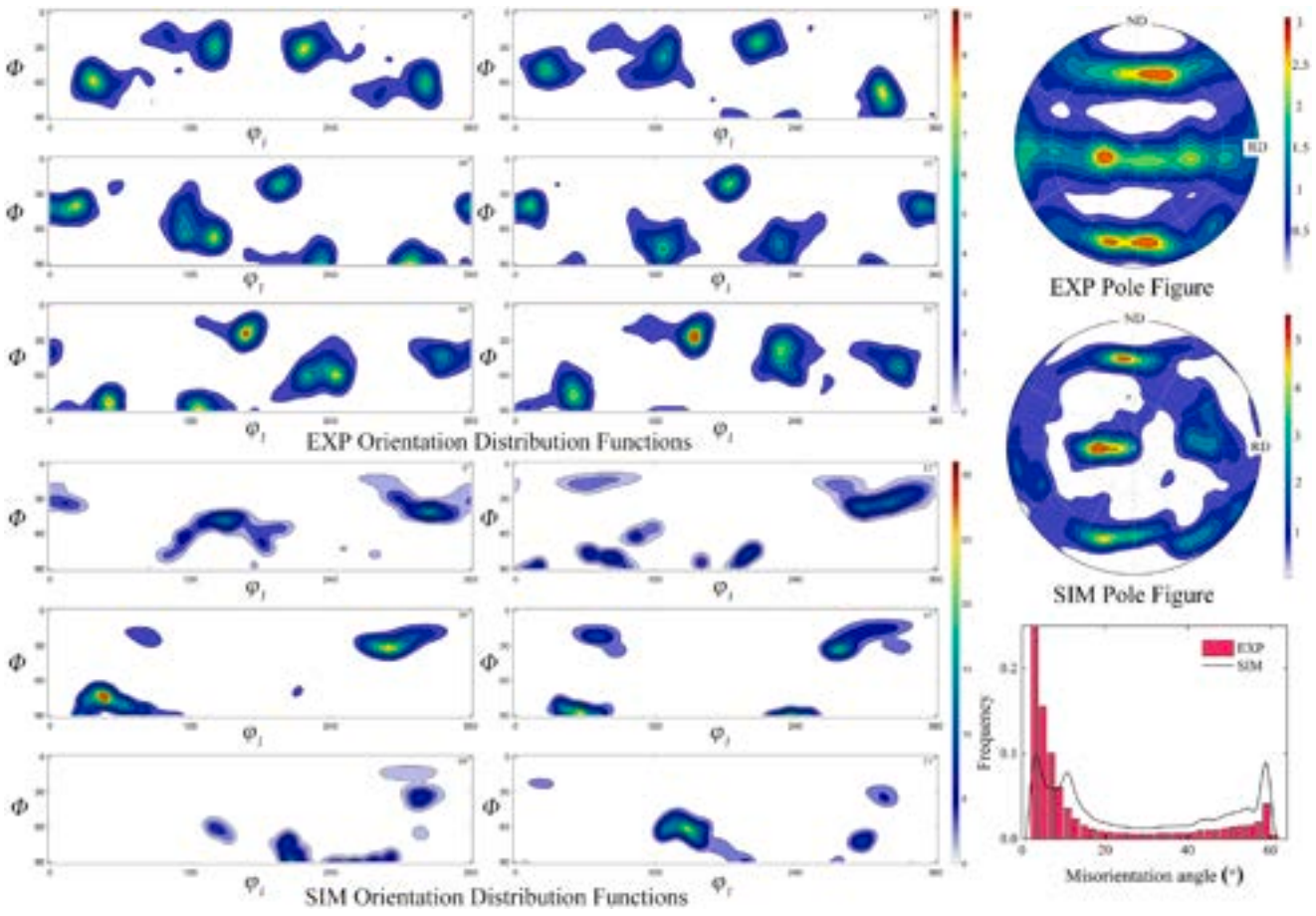

Fig. 15. Comparison of the experimental and CPFEM simulation orientation distribution functions, pole figures, and misorientation distribution functions of the MG sample.

III, specifically within the stroke range of 0.4–0.9 mm, only sliding friction between the punch and the shear-finished sheet material occurs. As a result, the load experiences fluctuations limited to tens of Newton. Therefore, an effective stroke from 0 to 0.4 mm is enough for the analysis. As shown in Fig. 12(c), the load first rises in step III and then experiences a slow increase and decrease during the continuous blanking process. After the cutting process is completed, the load abruptly drops to approximately 200 N, mainly generated by longitudinal sliding friction during the insertion of the part into the die tunnel. The maximum limit value for load in this progressive microforming system is 15,396 N, which is the sum of the individual maximum load values for each stage: 12,907 N from Step I, 2269 N from Step II, and 220 N from Step III. The CPFEM yields a similar prediction of (13,317+1828+355=) 15,500 N. This suggests that the new method can accurately predict the load limit.

The load-stroke curves exhibit various grain size effects. Firstly, the experimental results demonstrate that samples with smaller grains exhibit higher applied loads for the same stroke in every step. This trend is consistent with the conclusions in Section 4.1 as smaller grain size leads to increased stress. Secondly, the load for the FG sample shows an earlier steep increase compared to other grain sizes in Step I (forward extrusion), indicating a delayed occurrence of fracture. In 1972, Phillips and Armstrong [74] found that the fracture strain in brass materials (CuZn30) linearly decreased with $d^{-1/2}$. Nonetheless, this SE is much more pronounced in the simulation than in the experiment. Besides the steep rise, there are no significant differences in load between the other two larger grain sizes. Similarly, Zheng et al. [23] reported that the load-stroke curves in CuZn35 flat pogo pins with larger initial grain sizes (71 and 107 μm) were the same compared to smaller grain sizes. This indicates that there exists a threshold grain size beyond which the load-stroke response is not affected by the extrusion operation. Thirdly, at the initial stage of the experiment, the load for coarse-grained material tends to be greater but is quickly surpassed by that of fine-grained material when the stroke is less than 0.15 and 0.1 mm for Step I and III, respectively. This can be attributed to the difference in yield strain among different grain sizes. According to Li et al. [75], who synthesized the grain size effect on yield strain for brass CuZn30 material, there is an increase in yield strain from approximately 1.95×10^{-3} to 2.2×10^{-3} when the grain size decreases from CG to FG. While fine-grained material is still undergoing elastic deformation, coarse-grained material has already entered the plastic stage for the same stroke.

4.3. Size effect on product quality

The evaluation of the capability of CPFEM in predicting grain SEs in product quality was performed in several aspects. Firstly, dimensional accuracy, both in terms of heights and diameters, was assessed and compared with experimental measurements. Secondly, undesirable and asymmetric geometries were identified in CPFEM simulations and compared to actual product geometries. Lastly, surface defects and quality, including surface roughness, hole defects, etc., were analyzed and compared with experimental observations to ascertain the effectiveness of the CPFEM method in predicting grain SEs in product quality.

4.3.1. Size effect on microstructure and texture evolution

Given that the microstructure evolution is closely linked to dimensional accuracy and the formation of undesirable and asymmetric geometries [76], understanding the material flow behaviour in the

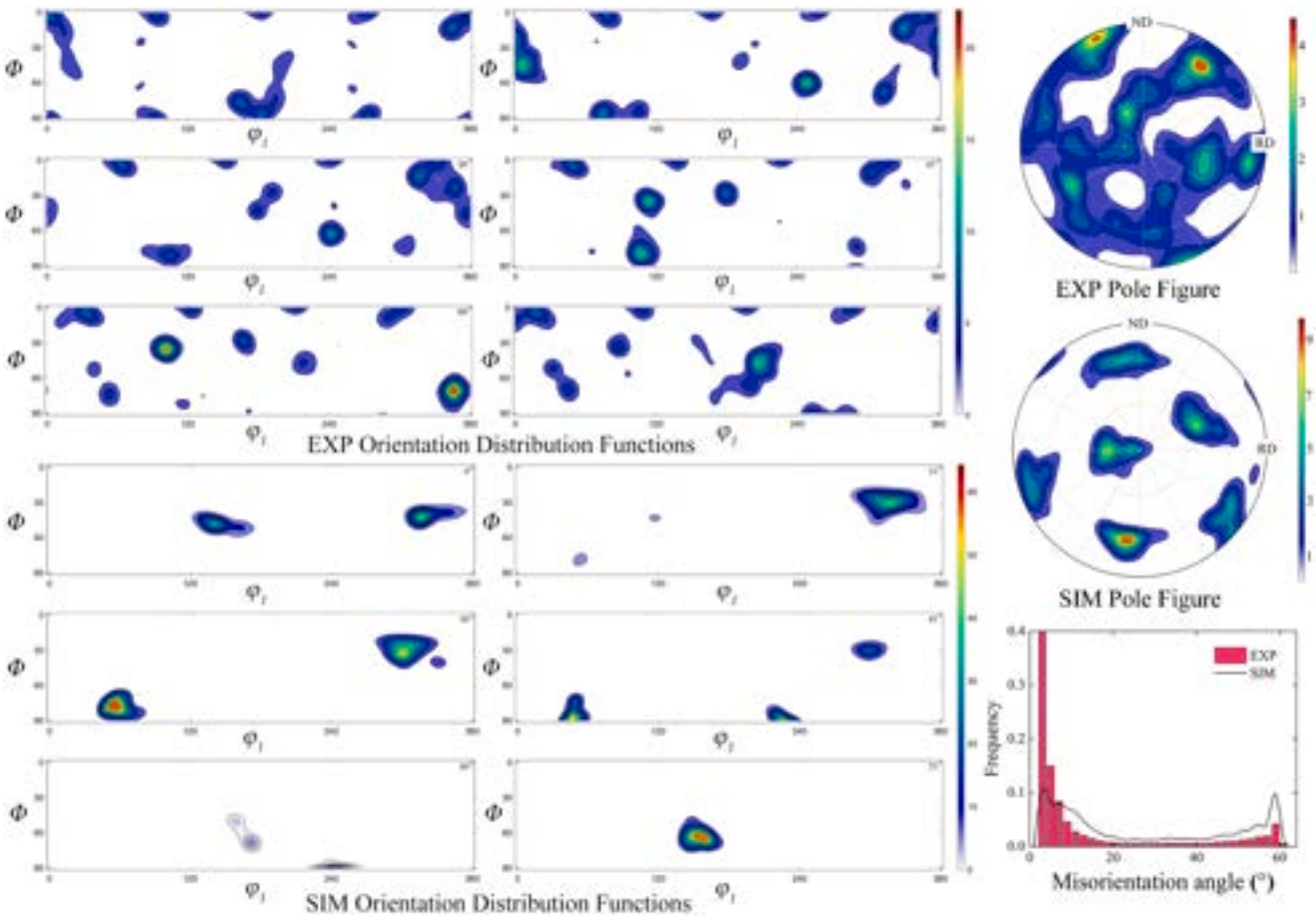

Fig. 16. Comparison of the experimental and CPFEM simulation orientation distribution functions, pole figures, and misorientation distribution functions of the CG sample.

progressive microforming process is crucial for optimizing the process and enhancing product quality [77]. Fig. 13 showcases the strain maps, texture changes, and microstructure of the cross-sections, highlighting the typical inferior geometry observed in the microformed parts with different initial grain sizes. It should be noted that the effective strain ε_{eq} in the conventional FEM can be directly extracted from software, while the effective strain ε_{eq} in the CPFEM simulation needs to be calculated following the equation [78]:

$$\varepsilon_{eq} = \frac{\gamma}{\sqrt{3}} = \frac{1}{\sqrt{3}}\left[(1-f^{tw})\sum_{\alpha}^{N^s}|\gamma^{\alpha}| + \sum_{\beta}^{N^{tw}}|\gamma^{\beta}|\right]. \tag{14}$$

The microstructural examination of the cross-sections of the resulting component reveals the presence of two prominent shear bands in which the material has undergone pronounced plastic deformation and flow, as shown in Fig. 13. Shear band I, which covers most of the head feature, was formed during the extrusion process in Step I and then continues to develop in Step II. This shear band also governs the material flow in the upper portion of the body. A gradual increase in the material flow line density becomes apparent when observing from the middle region of the head downwards. Shear band II, which was generated during the second operation, exhibits a higher flow line density in comparison to Shear band I. Shear band II appears as a series of lines of tens of micrometres, linking the bottom corner of the hexagonal socket feature to the junction between the shoulder and body portions. On both sides of the head region, four blanking shear bands were formed as a result of the second and third operations. Two friction shear bands also emerged due to extrusion and friction on both sides of the body feature. Regions with intense material flow, such as the shear bands, blanking shear bands, and friction shear bands, are more accurately predicted via the strain maps in CPFEM simulations than the conventional FEM. Elevated strain accumulations were observed in these regions, as illustrated in Fig. 13. However, the conventional FEM fails to maintain the continuity of strain distribution, resulting in a disjointed and unrealistic strain pattern. In addition to the aforementioned shear band regions, three dead metal zones were identified, located at the summit of both head regions, as well as the middle and lower portions of the body feature. Dead metal zones are characterized by a lack of material flow, with these three dead metal zones demarcated based on the extent of grain deformation, flow lines, and comparatively lower levels of strain accumulation as illustrated in Fig. 13. A comparison of the microstructures and flow patterns of the manufactured product with varying initial grain sizes reveals that the area occupied by shear bands decreases as the grain size increases, which contradicts the findings of Zheng et al. [23]. These shear bands and dead metal zones can also be roughly inferred from the texture of the CPFEM simulation results. The grains located in the shear band region underwent a large deformation, whereas the grains in the dead metal zones maintained their original shape.

To further validate the reliability of this CPFEM simulation, the comparisons of the experimental and CPFEM simulation orientation distribution functions (ODF), pole figures (PF), and MODF are given in Figs. 14–16 for FG, MG, and CG samples, respectively. Combining the ODFs and the PFs, the relative consistency of the orientation distributions in the experimental and simulation results can be observed and is particularly evident for FG and MG samples. However, the crystal orientations show higher degree of concentration in the simulations. The difference is because the number of grains involved in the simulation is less than that in the experiment. The overall changes in the textures were

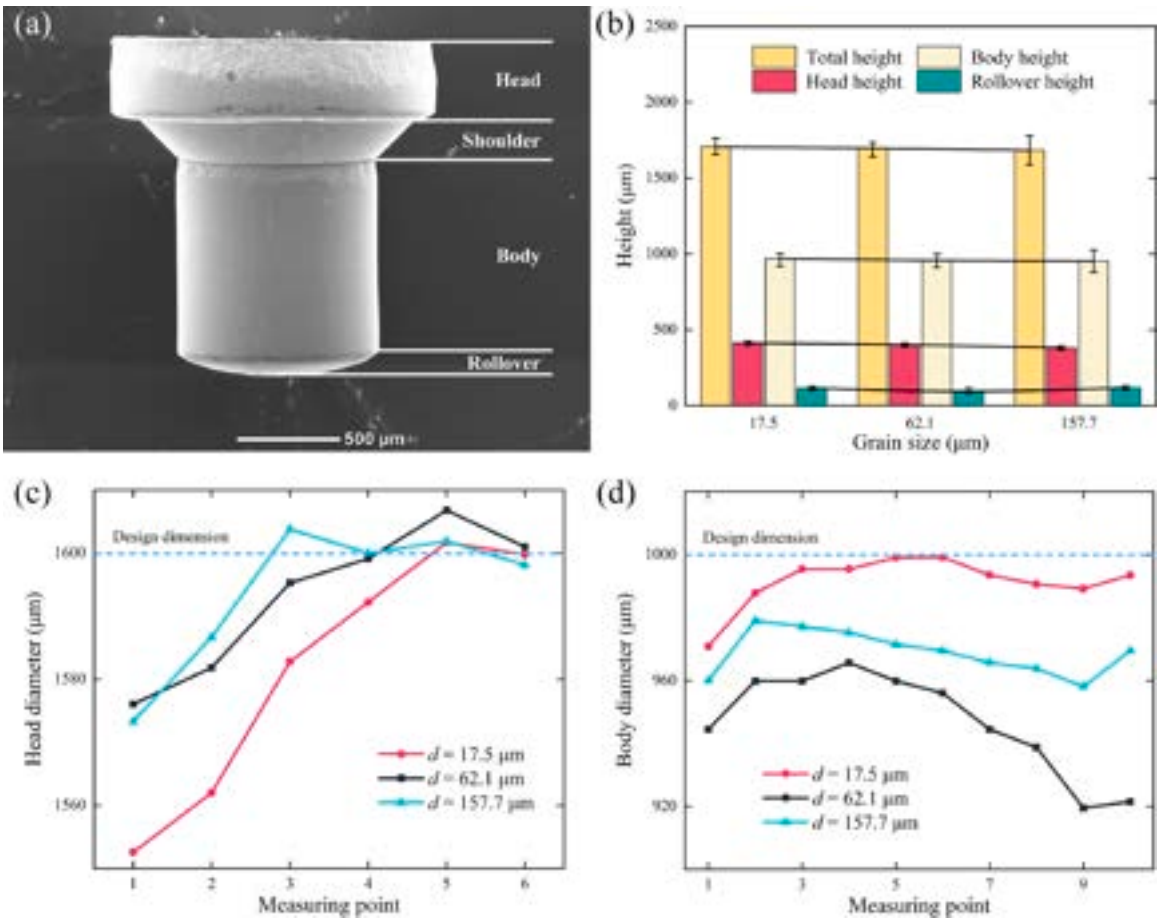

Fig. 17. (a) The SEM image of the fabricated part indicates several features: head, shoulder, body, and rollover. (b) The average values and errors of the heights of these features for each grain size. (c) The head diameter measurements from top to bottom with the design dimension of 1600 μm for each grain size. (d) The body diameter measurements from top to bottom with the design dimension of 1000 μm for each grain size.

very dramatic because of the complexity of the process when comparing the initial texture (Fig. 2) and the deformed texture (Figs. 14–16). After two extrusion and one blanking operations, the preference for anisotropic texture can be observed for the FG and MG cases, as shown in Figs. 14 and 15, which is very similar to the compressed α-brass texture [58]. In contrast, the CG sample shows a more isotropic texture, in which the maximum density reaches 9.87 and the maximum values for FG and MG samples are only 5.62 and 6.05 in the PFs. This indicates that the grain size plays an important role in the texture evolution. In the head and body of the product, the interactions among grains during deformation, particularly between surface and internal grains, are minimal with the presence of coarse grains. Considering the dead metal zones in the middle of the body feature, for instance; the grains in this zone experienced minimal deformation but exhibited pronounced rotating. For the CG material, the tilting of these grains is more diversified, whereas for the FG and MG materials, the deformation tends to follow a specific pattern.

In addition, there is a partial agreement and variability between the resulted experimental and simulation MODFs. Comparing the initial and resultant MODFs (Fig. 8 and Figs. 14–16), the proportion of misorientations around 60° is greatly reduced, while the fraction of low-angle grain boundaries (LAGBs) grows dramatically. The increase in LAGBs is very common during compression [79]. However, the ratio of LAGBs in the simulation results is not as high as in the experimental results because a large amount of grain fragmentation and sub-grain boundaries were produced in physical experiments. In summary, the reliability and validity of this CPFEM simulation method can be verified by comparing and analyzing the ODFs, PFs, and MODFs in the experimental and simulation results.

4.3.2. *Size effect on dimensional accuracy*

The material anisotropy arising from the microstructure and texture leads to inhomogeneous deformation, which becomes increasingly pronounced with the grain size [80]. To determine and compare the SEs on dimensional accuracy, the height and diameter distributions of key features of the hexagonal socket part were examined, as depicted in Fig. 17. The part was divided into head, shoulder, body, and rollover features from top to bottom (Fig. 17(a)). The rollover, a common irregular geometry in extruded parts, was formed in the first step of this progressive microforming process and will be discussed in Section 4.3.2. Firstly, the heights of each feature were collected from the SEM results and cross-section images, as shown in Fig. 17(b). Based on the data, two grain SEs can be summarized: (a) the scatter of every feature height increases with grain size; (b) except for rollover, the heights of all features decrease with the increasing grain size. These observations are consistent with the conclusions of prior research by Tang et al. [24]. Based on the microstructure and texture evolution shown in Figs. 13–16, the grain orientations gradually concentrate to several specific directions according to the pole figures. For the finer-grained and medium-grained materials, the concentration of crystal orientations is higher, resulting in more radial material flow and higher heights of the product. The design dimension for the total height of the part was set as 1.7 mm. During testing, the actual measurement error was found to be ± 0.02 mm, which falls within the acceptable limit. Secondly, the head and body diameters were evaluated experimentally and showed different levels of scattering (Fig. 17(c-d)). The head diameter distribution

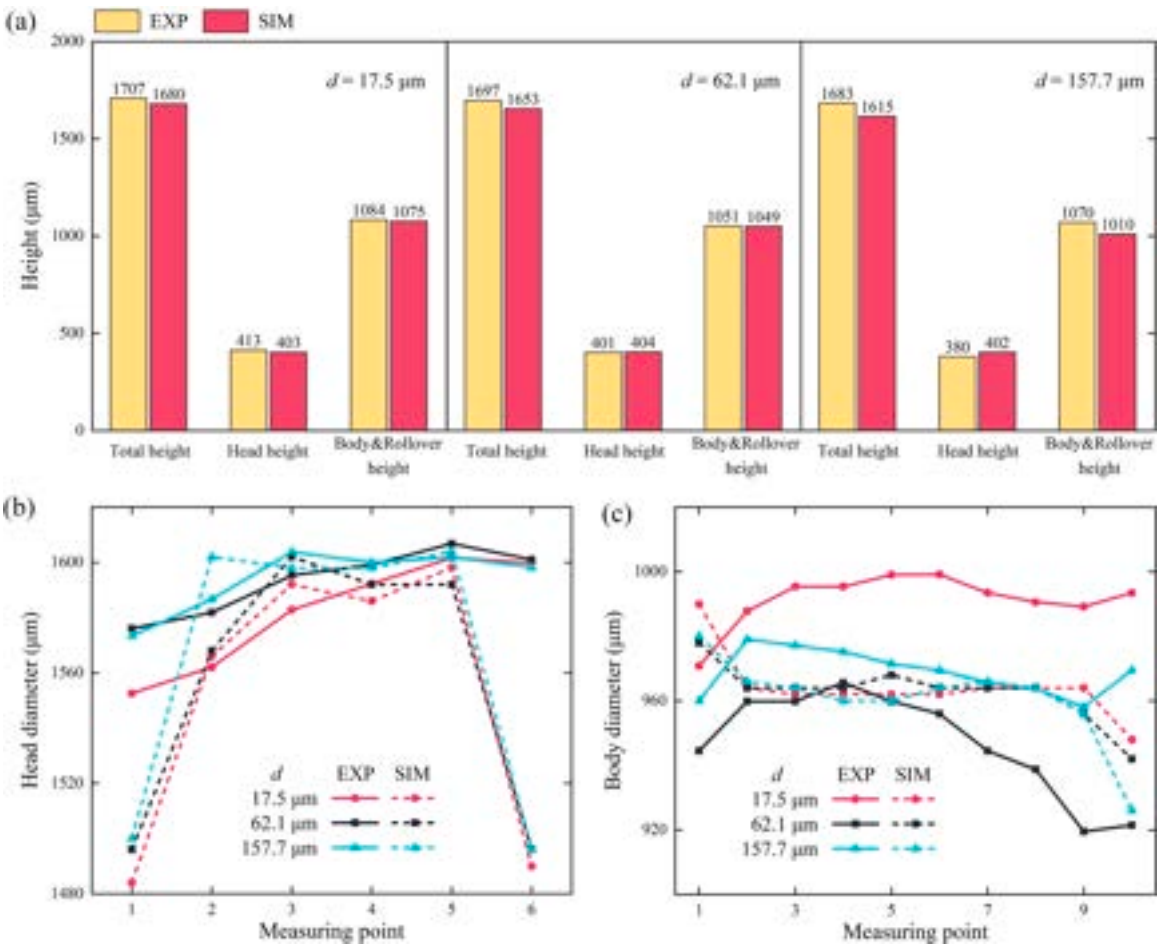

Fig. 18. The comparison of the important feature sizes in simulation and experiment results. (a) The heights of the head, body, and rollover, and whole part for different grain sizes are collected and compared. (b)-(c) The assembly dimensions, that is, the diameters of the head and body features, are measured from top to bottom and compared.

displayed a gradual rising trend from top to bottom. The measured error was found to be substantial when compared to the design dimension of 1.6 mm due to irregular material fracture in the upper region. Thirdly, the body diameter showed an initial increase followed by a gradual decrease with a slight increase at the junction with the rollover feature. The design dimension for the body diameter is 1 mm, and the results are deemed acceptable only for the FG case since the dimension differences reach 4 and 8 % for MG and CG samples, respectively. The abrupt change in diameter at the topmost measuring point is a consequence of necking that occurs during the second step of the process.

Fig. 18 provides a comparative analysis of feature dimensions in both experiments and simulations with varying grain sizes. The simulation results directly determine heights, as demonstrated in Fig. 13, while the diameters are twice the values mentioned earlier. Due to the lack of distinct boundaries between the body and rollover features in the simulation results, their heights were integrated for analytical purposes. As shown in Fig. 18(a), major differences in overall height arise from variations in the body and rollover dimensions, while the head heights remain consistent. The inclusion of burr geometry, which was not considered in the simulation results, significantly contributes to overall height. The simulation results exhibit a slight underestimation of the experimental height, and this discrepancy becomes more pronounced for coarser-grained materials. This discrepancy can be attributed to an increase in transverse material flow and a decrease in extrudate height caused by the presence of coarse grains. In the case of a limited number of grains in the direction of sheet thickness, the presence of grain inhomogeneity results in unfavourable material flow directions that deviate from the intended punching direction. As depicted in Fig. 18(b), the simulation results indicate a decrease in head diameters with the rising grain size. The middle region of the head demonstrates minimal deviation from the experimental results, while the ends show significant decreases. In contrast to the head diameters, the simulation results do not reveal significant grain SEs on the body diameter distributions. However, the experimental results show a decrease followed by an increase in the body diameter with grain size (Fig. 18(c)). Interfacial friction, despite the use of identical machine oil as a lubricant, is also considered a contributing factor to grain SEs. In summary, the dimensional accuracy of the CPFEM predictions is satisfactory, with corresponding grain SEs being adequately reflected. However, Fig. 13 further highlights the shortcomings of the conventional FEM simulations in predicting the total heights, with an error of 0.1 mm and a slight overestimation of the rollover feature height.

4.3.3. Size effect on undesirable and asymmetric geometries

The degree of asymmetry exhibited by the final component is notably pronounced and is particularly conspicuous in the cross-sections of the samples, as presented in Fig. 13. Given the left-right symmetry of the formed part, the asymmetry primarily manifests in two ways: (1) the disparity in the horizontal distance of equivalent structures from the central axis, and (2) the differential in the elevational height of equivalent structures. The positioning of the material during the experiment is contingent upon the conformity of the dies and prior feature configurations, as well as the regulation of the feeding mechanism. In the progressive microforming process, the inadequate design of tooling

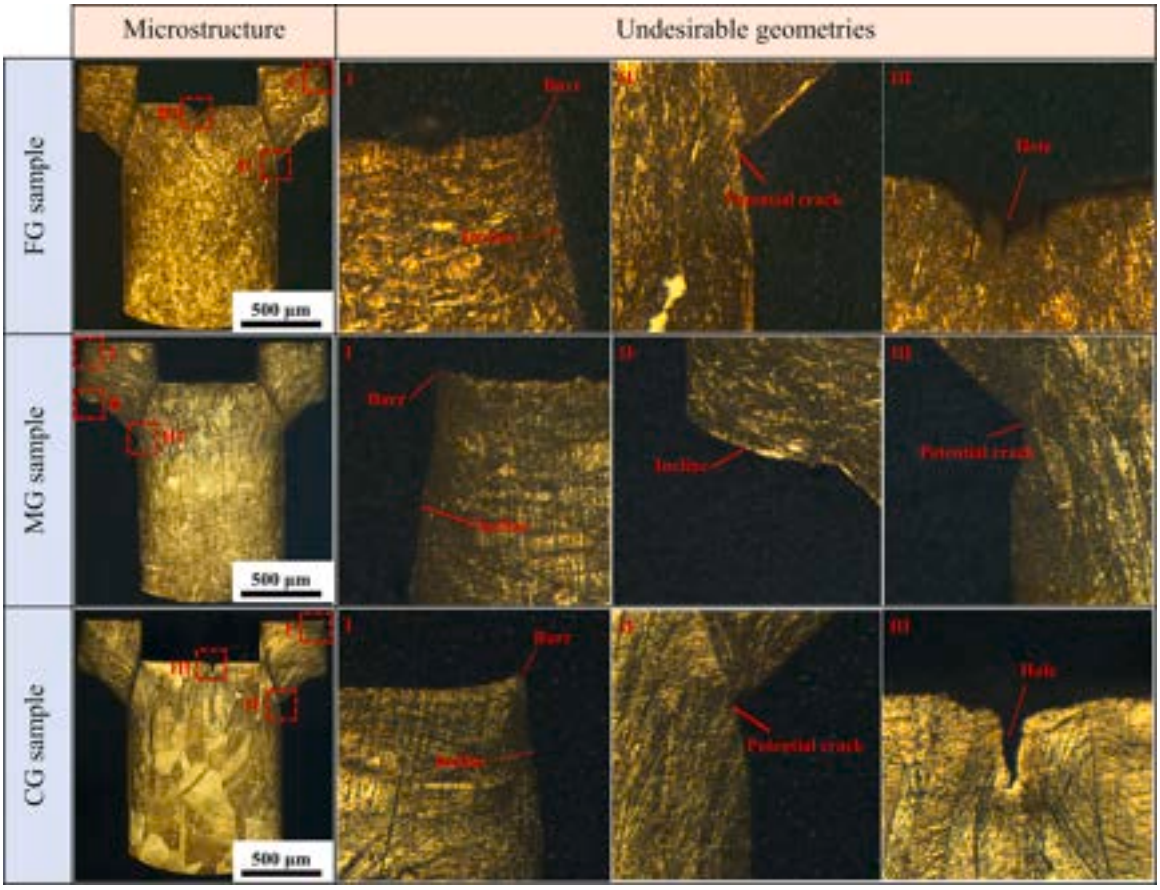

Fig. 19. Various undesirable geometries for the FG, MG, and CG samples, including burr, incline, potential crack, and hole.

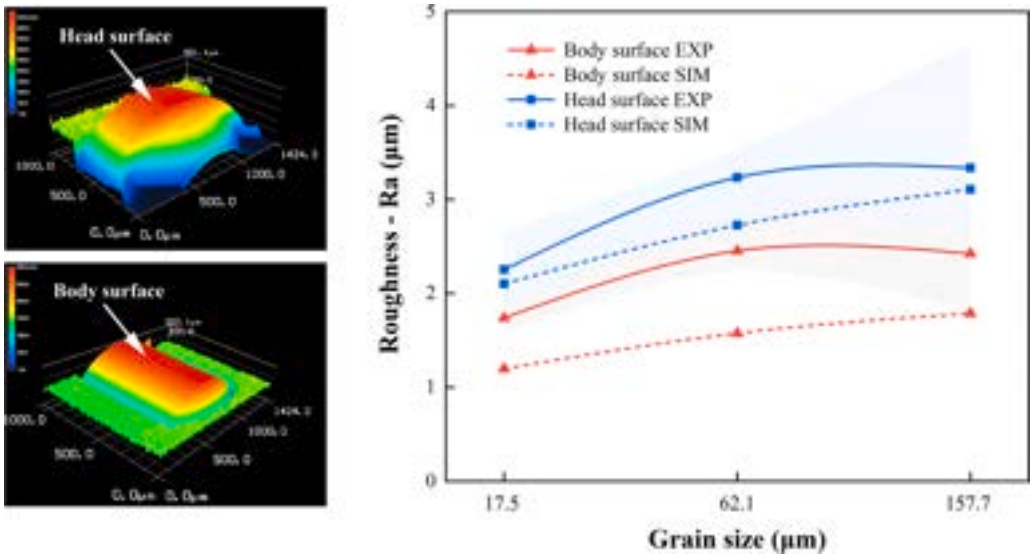

Fig. 20. The surface roughness measurement mappings of the head and body surfaces. The simulation results are calculated via Eq. (15), and the shaded areas represent the calculation errors in simulation results. Then the surface roughness in experimental and simulated results are drawn and compared.

tolerance and feeding velocity can lead to asymmetrical results, posing a significant challenge for simulation purposes. Addressing this challenge requires a two-fold approach: reducing clearances and enhancing the accuracy of fit [81].

The present study has identified several undesirable geometries in the formed part, including burrs, inclines, rollovers, and holes, as depicted in Fig. 19. The phenomenon of rollover is a direct consequence of the extrusion of micro grains in the first operation. The CPFEM approach outperforms conventional FEM in accurately predicting this phenomenon, as conventional FEM overestimates the rollover height. The burr and the first incline appear on the top corner and side surfaces of the head feature during the third step. The clearance between the punch and the die in the third step is extremely small, within 0.01 mm, which precludes the presence of grain SE in the burrs. However, the

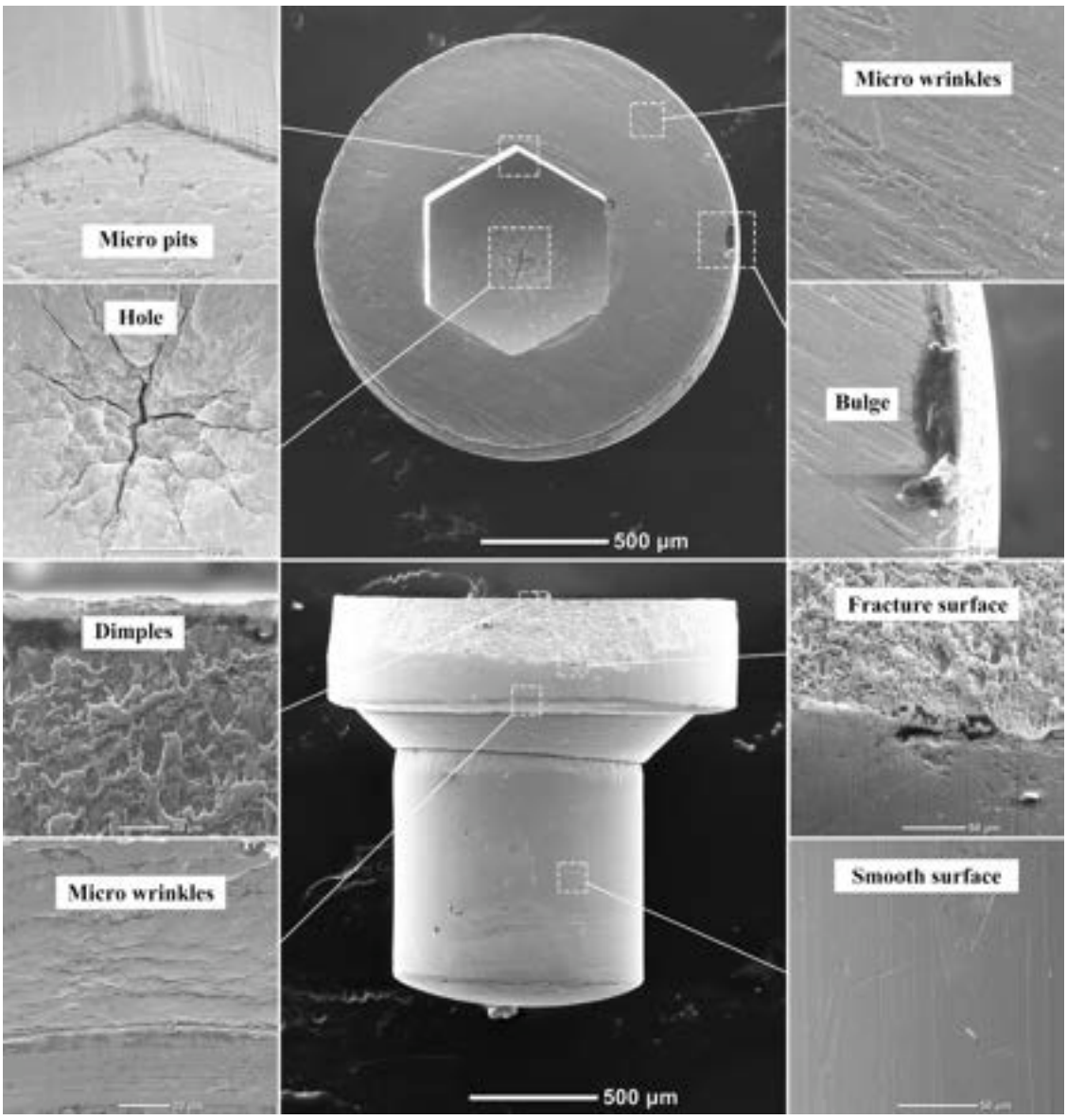

Fig. 21. SEM images and surface morphology of the hexagonal socket parts for FG sample. Some surface flaws are observed, including wrinkles and bulges on the top surface of the head, micro pits and holes on the bottom surface of the socket, and dimples and fracture surfaces on the side surface of the head.

measurements of head diameters, as shown in Fig. 18**(b)**, indicate that the incline angle increases with the reduction in grain size due to the difficulties in squeezing coarser grains into the gaps between the punch and die. The second incline on the bottom corner of the head feature is due to the friction between the material and the die. The potential crack was produced by shearing between the body and head material during Step II. It constitutes a crucial defect that requires subsequent process adjustments. However, the burrs were not accurately predicted by CPFEM simulations. As shown in Fig. 19, the hole/piping defect is regarded as a common defect that occurs during the forward extrusion process [82]. The hole forms during the initial extrusion step when material flows rapidly radially into the extrusion die, leading to an axial hole in the middle area on the back end of the extruded material. Balasundar and Raghu [83] reported that the formation and size of this hole were related to the chamfer angle, extrusion height, and friction conditions. The present study has discovered the relationships between the hole defect and material microstructure that the width of the hole is smaller and the depth is deeper in coarser-grained material, while the position of the hole moves away from the center point with increasing grain size, as depicted in Figs. 21–23. CPFEM simulation demonstrates a notable capability in predicting hole defects, which is also a critical feature in progressive micromanufacturing, although it may generate larger hole sizes compared to the actual case. On the other hand, conventional FEM does not exhibit significant tendencies towards the formation of these defects.

4.3.4. *Size effect on surface defects and quality*

To study the grain SEs on surface roughening, the morphology of the surfaces on the hexagon socket part was observed by SEM, and the surface roughness was measured by using a 3D laser scanning microscope. Fig. 20 shows the measuring location and results of the roughness. The side surfaces of the head and body features were selected as the measurement locations, which were first tilted by an accompanying software to transform them into a plane. The roughness R_a was calculated by node coordinates obtained from the CPFEM simulation results according to:

$$R_a = \frac{1}{n}\sum_{i=1}^{n}|h_i - \overline{h}|. \tag{15}$$

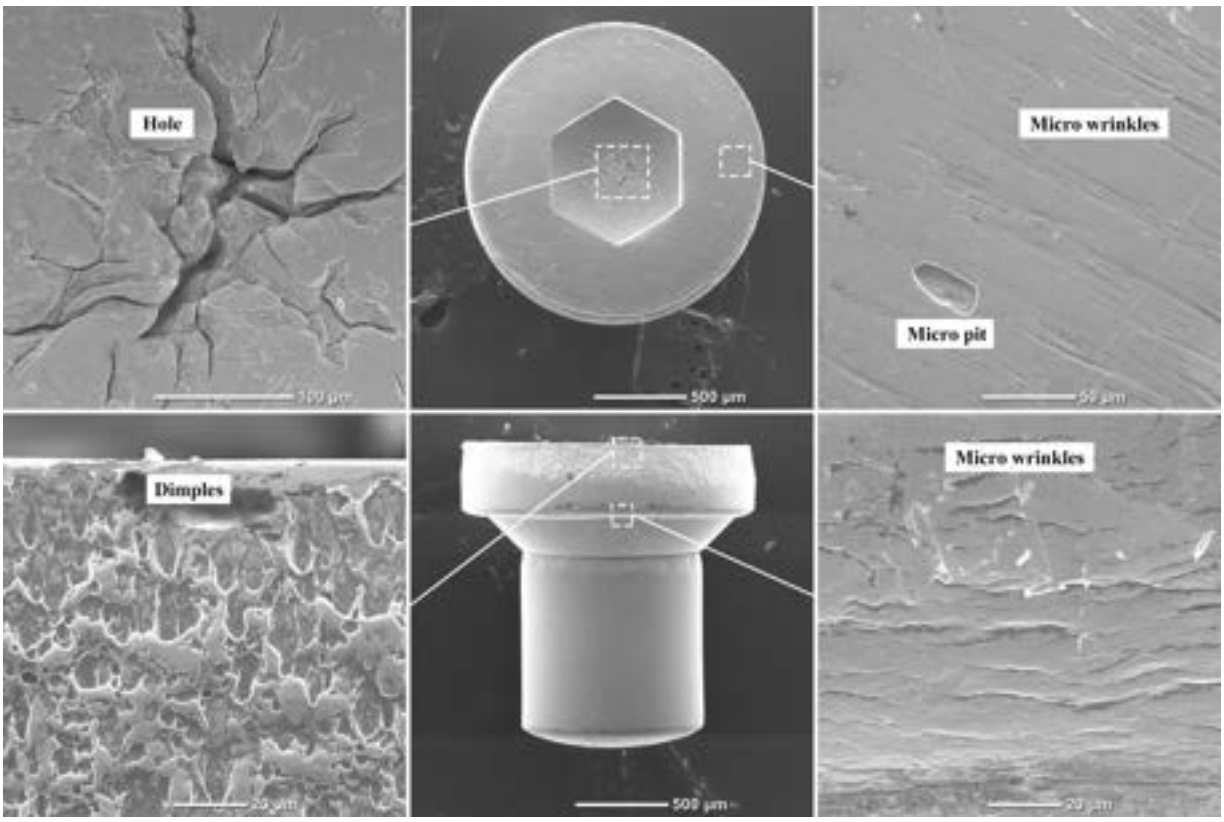

Fig. 22. SEM images and surface morphology of the hexagonal socket parts for MG sample. Some surface flaws are observed, including wrinkles and pits on the top surface of the head, holes on the bottom surface of the socket, dimples and fracture surface on the side surface of the head.

Here h_i represents the distance between the selected nodes on the measuring surface and the central axis. $\overline{h}$ is the average value of h_i.

Fig. 20 demonstrates the disparity in roughness between the head surface and the body surface, which is primarily attributed to the different mechanisms. The head surface is characterized by the formation of a blanking shear band, as opposed to the friction shear band that constitutes the body surface. An examination in Fig. 21 reveals that the upper reaches of the head surface are distinctly characterized by the presence of a fracture surface feature, resulting from the material blanking process and resulting in a concomitant enhancement of roughness. In contrast, the body surface exhibits a notably smooth appearance, with minimal irregularities, except for the occurrence of a few sporadic longitudinal fine lines. These fine lines can be attributed to the relative sliding between the material and the die during the manufacturing process. It is also observed that the surface roughness is positively correlated with the grain size. The trend mentioned above is evident in the results obtained from the CPFEM simulations, albeit with magnitudes smaller in comparison to the experimental findings. The anisotropy of the grains induces incompatible strains within neighbouring grains, leading to a scenario where certain grains undergo vertical deformation while others deform in different orientations. This phenomenon ultimately gives rise to a rough surface. As the grain size increases, the surface grains are subjected to lower constraints, leading to more severe incompatible deformation of those grains and a corresponding increase in surface roughness. The error in the simulation results (shaded area) also increases with the grain size for the same reason. Moreover, the surface roughness is intricately related to the lubrication conditions. For a given sheet thickness, when the grain size increases, it leads to a reduction in the presence of lubrication pockets, resulting in an increase in friction and surface roughness [84]. In conclusion, the roughness of the formed part is significant, and the performance of the fine-grained materials is comparatively superior. Efforts towards improving the product surface quality, such as further surface treatment of the tooling and optimized lubrication conditions, are imperative.

To study the distribution and presence of specific surface defects on the hexagon socket part, SEM was employed. Figs. 21–23 depict a range of flaws, including micro pits, dimples, micro wrinkles, bulges, and holes. While the surfaces of the body and rollover exhibit relatively smooth textures resulting from forward extrusion occurring parallel to the punch stroke direction, fracture surfaces covering close to half of the head side surface were discovered during the examination. The presence of dimples on the head surfaces indicates ductile fracture induced by shear stress. It was observed that the number of dimples decreased with increasing grain size, while the average size of dimples increased, which is consistent with the research of Su et al. [85]. This is due to the ease of dislocation movements and slips at grain boundaries, leading to the formation of dimples with high energy absorption during coordinated deformation [86]. The lower boundaries of the fracture surfaces were found to be irregular and uneven, leading to large roughness on the surface. It was discovered through examination that the head feature of the subject material possessed distinct micro wrinkles of varying morphologies on both its upper and lower surfaces. The formation of the micro wrinkles on the lower surface was attributed to the initial stage of extrusion, where the self-extrusion of the material in conjunction with the friction generated by the die led to the creation of defects of varying lengths perpendicular to the direction of the punch stroke. It was discovered that an increase in grain size resulted in the reduction of wrinkles, leading to a smoother surface. Conversely, the formation of micro wrinkles on the upper surface of the head predominantly occurs as a consequence of the relative sliding between the material and punch during the initial stage. These wrinkles were exclusively observed in the outer circle of the head and were always parallel to the feed direction in the progressive microforming system. It was previously reported that these micro wrinkles (or scratches) could be prevented by optimizing lubrication conditions [87]. In addition to the aforementioned wrinkles,

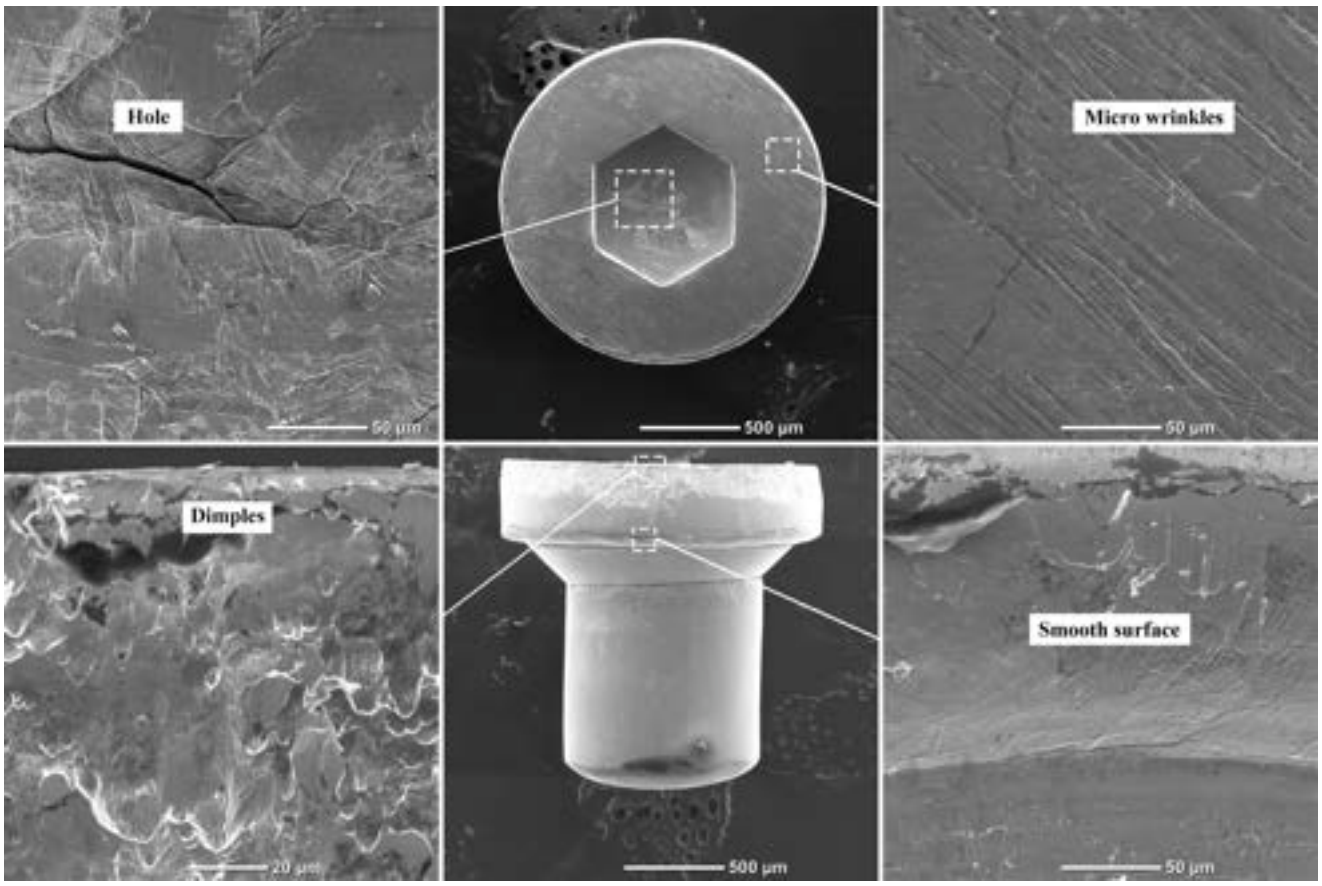

Fig. 23. SEM images and surface morphology of the hexagonal socket parts for CG sample. Some surface flaws are observed, including wrinkles on the top surface of the head, holes on the bottom surface of the socket, large dimples and fracture surface on the side surface of the head.

micro pits were observed on the bottom surface of the hexagon socket adjacent to the hole. These micro pits were also caused by the extrusion of the material and punch and were found to be sporadically distributed and of small size.

The hole defect was found to possess another grain SE observable from the SEM figures that as the grain size increases, the number of diffusing "branches" around the hole decreases. These "branches" are cracks formed by the coalescence of voids at high-stress locations near grain boundaries. The reduction in grain size leads to an increase in the volume fraction of the grain boundaries, which correspondingly increases the crack density. In conclusion, the presence of dimples on the side surface of the head, micro wrinkles on the lower surface of the head, and holes on the bottom surface of the hexagon socket show significant grain size tendencies, while the other surface defects did not exhibit such a correlation. It is challenging to directly determine the aforementioned surface defects from the CPFEM simulations. Their presence was primarily inferred from roughness measurements in the simulations.

5. Conclusions

In this study, a novel CPFEM and CZM method was developed to investigate the deformation and failure behaviours induced by grain SEs in uniaxial tensile tests and progressive microforming. The CPFEM model incorporates the effects of slip and twinning on deformation behaviour in brass materials, while the CZM considers the separation of material through the adoption of the bi-linear TSL and MAXS criterion. RVEs with actual textures of CuZn32 materials of various grain sizes were simulated and validated the results with uniaxial tensile tests. The mechanical response of the material, which obeys the Hall-Petch relation, is in good agreement with the experimental results.

This study implements a three-step progressive microforming process to produce a hexagonal socket part and evaluate the prediction capability of the CPFEM method on the grain size effects in stress and strain distribution, microstructure and texture evolution, deformation load, dimensional accuracy, irregular geometries, and surface quality. The CPFEM method accurately predicts the deformation load limit with different grain sizes, and consistently delivers results that match experimental observations in terms of dimensional accuracy and grain SEs. The total height of the part increases as grain size decreases, while the head diameter rises with grain size. It is proven that the part with the initial fine-grained material has the best fit with the design scenarios in terms of its feature sizes.

The microstructure and texture evolution during progressive microforming is revealed through the observations of the cross-sections of the part. By comparing the ODFs, PFs, and MODFs in the experimental and simulation results, the reliability of this CPFEM approach was validated. The shear bands and dead metal zones are properly predicted in the strain maps created in CPFEM simulations, with the size of the dead metal zones expanding as the grain size becomes coarser. Hole and rollover geometries can be identified, but differences arise for burr and incline geometries. The grain size-induced hole defects were found to have more branches and become narrower and deeper with the increase in grain size. Other surface defects, including dimples, micro pits, and micro wrinkles, were found to be more prominent in coarser-grained materials, but identification from CPFEM simulation results can be challenging. However, their presence can be inferred from surface roughness analysis in simulation results.

To conclude, this CPFEM method offers a strong approach for simulating and predicting complex micro/meso-scale forming processes involving elastic deformation, plastic deformation, and fracture. This

methodology has the potential to improve constitutive models for various materials and the distribution of cohesive elements for different processes and products in future research.

Availability of data and material

All the data and material are available upon request to the corresponding authors.

Data availability

Data will be made available on request.

Funding

Xu TONG and M.W. FU would like to acknowledge the funding support from the National Natural Science Foundation of China with project No. 51835011 and project No. 15223520 from the General Research Fund of Hong Kong, and project No. 1-ZE1W from the Hong Kong Polytechnic University. Yan LI would like to acknowledge the funding support from the National Science Foundation under Award # OIA-2218063, as well as the start-up funds from Thayer School of Engineering at Dartmouth College.

CRediT authorship contribution statement

Xu Tong: Conceptualization, Methodology, Software, Data curation, Visualization, Writing – original draft. **Yan Li:** Conceptualization, Writing – review & editing. **M.W. Fu:** Supervision, Writing – review & editing, Project administration, Funding acquisition.

Declaration of competing interest

The authors declare that they have no known competing financial interests or personal relationships that could have appeared to influence the work reported in this paper.

References

[1] Ghassemali E, Tan MJ, Jarfors AEW, Lim SCV. Optimization of axisymmetric open-die micro-forging/extrusion processes: an upper bound approach. Int J Mech Sci 2013;71:58–67. https://doi.org/10.1016/j.ijmecsci.2013.03.010.
[2] Xu Z, Qiu D, Shahzamanian MM, Zhou Z, Mei D, Peng L. An improved springback model considering the transverse stress in microforming. Int J Mech Sci 2023;241:107947. https://doi.org/10.1016/j.ijmecsci.2022.107947.
[3] Fu MW, Wang JL. Size effects in multi-scale materials processing and manufacturing. Int J Mach Tools Manuf 2021;167:103755. https://doi.org/10.1016/j.ijmachtools.2021.103755.
[4] Thompson ST, James BD, Huya-Kouadio JM, Houchins C, DeSantis DA, Ahluwalia R, Wilson AR, Kleen G, Papageorgopoulos D. Direct hydrogen fuel cell electric vehicle cost analysis: system and high-volume manufacturing description, validation, and outlook. J Power Sources 2018;399:304–13. https://doi.org/10.1016/j.jpowsour.2018.07.100.
[5] Kraus M, Merklein M, Daehn G, Cao J, Kinsey B, Tekkaya E, Vivek A, Yoshida Y. Bulk microforming from sheet metal—a promising approach for the mass production of cold-formed metallic micro parts. Forming the future. Cham: Springer International Publishing; 2021. p. 151–65. https://doi.org/10.1007/978-3-030-75381-8_12.
[6] Ran JQ, Xu L, Wang JL, Xu T, Gong F. Influence of dead metal zone on dislocation strengthening effect during micro-progressive forming. Int J Adv Manuf 2019;105:1129–41. https://doi.org/10.1007/s00170-019-04147-6.
[7] Xu Z, Li Z, Zhang R, Jiang T, Peng L. Fabrication of micro channels for titanium PEMFC bipolar plates by multistage forming process. Int J Hydrog Energy 2021;46:11092–103. https://doi.org/10.1016/j.ijhydene.2020.07.230.
[8] Wang J, Xiao Z, Wang X, Sun Y, Sun C. Ductile fracture behavior in micro-scaled progressive forming of magnesium-lithium alloy sheet. Int J Adv Manuf 2022;121:967–80. https://doi.org/10.1007/s00170-022-09370-2.
[9] Yang Y, Hinduja S. Sequence planning of sheet metal parts manufactured using progressive dies. Int J Adv Manuf 2023;124:2199–214. https://doi.org/10.1007/s00170-022-10389-8.
[10] Ghassemali E, Tan MJ, Jarfors AEW, Lim SCV. Progressive microforming process: towards the mass production of micro-parts using sheet metal. Int J Adv Manuf 2013;66:611–21. https://doi.org/10.1007/s00170-012-4352-4.
[11] Wang Y, Zheng Z, Zeng F, Fu M. Geometrical and microstructural size effects in progressive forming using wires. Int J Mech Sci 2023;251:108332. https://doi.org/10.1016/j.ijmecsci.2023.108332.
[12] Pradeep Raja C, Ramesh T. Influence of size effects and its key issues during microforming and its associated processes – a review. Eng Sci Technol Int J 2021;24:556–70. https://doi.org/10.1016/j.jestch.2020.08.007.
[13] He W, Wan M, Meng B. Size effect on nonlinear unloading behavior and Bauschinger effect of Ni-based superalloy ultrathin sheet. Int J Mech Sci 2022;231:107563. https://doi.org/10.1016/j.ijmecsci.2022.107563.
[14] Uchida M, Tsutsumi K, Sakamoto M, Kaneko Y. Characterization of size-affected non-uniform deformation of polycrystalline copper. Int J Mech Sci 2021;211:106760. https://doi.org/10.1016/j.ijmecsci.2021.106760.
[15] Meng B, Cao BN, Wan M, Xu J, Shan DB. Ultrasonic-assisted microforming of superalloy capillary: modeling and experimental investigation. J Manuf Process 2020;57:589–99. https://doi.org/10.1016/j.jmapro.2020.07.015.
[16] Xu Z, Peng L, Lai X. Investigation on the roll-to-plate microforming of riblet features with the consideration of grain size effect. Int J Adv Manuf 2020;109:2055–64. https://doi.org/10.1007/s00170-020-05687-y.
[17] Chan WL, Fu MW. Experimental and simulation based study on micro-scaled sheet metal deformation behavior in microembossing process. Mater Sci Eng A 2012;556:60–7. https://doi.org/10.1016/j.msea.2012.06.058.
[18] Fu MW, Chan WL. Micro-scaled progressive forming of bulk micropart via directly using sheet metals. Mater Des 2013;49:774–83. https://doi.org/10.1016/j.matdes.2013.02.045.
[19] Chan WL, Fu MW. Meso-scaled progressive forming of bulk cylindrical and flanged parts using sheet metal. Mater Des 2013;43:249–57. https://doi.org/10.1016/j.matdes.2012.07.004.
[20] Zhang R, Xu Z, Peng L, Lai X, Fu MW. Modelling of ultra-thin steel sheet in two-stage tensile deformation considering strain path change and grain size effect and application in multi-stage microforming. Int J Mach Tools Manuf 2021;164:103713. https://doi.org/10.1016/j.ijmachtools.2021.103713.
[21] Meng B, Fu MW, Fu CM, Wang JL. Multivariable analysis of micro shearing process customized for progressive forming of micro-parts. Int J Mech Sci 2015;93:191–203. https://doi.org/10.1016/j.ijmecsci.2015.01.017.
[22] Zheng JY, Yang HP, Fu MW, Ng C. Study on size effect affected progressive microforming of conical flanged parts directly using sheet metals. J Mater Process Technol 2019;272:72–86. https://doi.org/10.1016/j.jmatprotec.2019.05.007.
[23] Zheng JY, Shi SQ, Fu MW. Progressive microforming of pin-shaped plunger parts and the grain size effect on its forming quality. Mater Des 2020;187. https://doi.org/10.1016/j.matdes.2019.108386.
[24] Tang XF, Shi SQ, Fu MW. Interactive effect of grain size and crystal structure on deformation behavior in progressive micro-scaled deformation of metallic materials. Int J Mach Tools Manuf 2020;148. https://doi.org/10.1016/j.ijmachtools.2019.103473.
[25] Esmaeilpour R, Kim H, Park T, Pourboghrat F, Xu Z, Mohammed B, Abu-Farha F. Calibration of Barlat Yld2004-18P yield function using CPFEM and 3D RVE for the simulation of single point incremental forming (SPIF) of 7075-O aluminum sheet. Int J Mech Sci 2018;145:24–41. https://doi.org/10.1016/j.ijmecsci.2018.05.015.
[26] Singh J, Kim MS, Choi SH. The effect of initial texture on micromechanical deformation behaviors in Mg alloys under a mini-V-bending test. Int J Plast 2019;117:33–57. https://doi.org/10.1016/j.ijplas.2018.01.008.
[27] Raj A, Verma RK, Singh PK, Shamshoddin S, Biswas P, Narasimhan K. Experimental and numerical investigation of differential hardening of cold rolled steel sheet under non-proportional loading using biaxial tensile test. Int J Plast 2022;154:103297. https://doi.org/10.1016/j.ijplas.2022.103297.
[28] Roters F, Eisenlohr P, Hantcherli L, Tjahjanto DD, Bieler TR, Raabe D. Overview of constitutive laws, kinematics, homogenization and multiscale methods in crystal plasticity finite-element modeling: theory, experiments, applications. Acta Mater 2010;58:1152–211. https://doi.org/10.1016/j.actamat.2009.10.058.
[29] Chakrabarty A, Chakraborty P, Jain R, Sahu VK, Gurao NP, Bar HN, Khutia N. Influence of scanning and building strategies on the deformation behavior of additively manufactured AlSi10Mg: CPFEM and finite element studies. Met Mater Int 2023. https://doi.org/10.1007/s12540-023-01418-6.
[30] Zhang W, Hu Y, Ma X, Qian G, Zhang J, Yang Z, Berto F. Very-high-cycle fatigue behavior of AlSi10Mg manufactured by selected laser melting: crystal plasticity modeling. Int J Fatigue 2021;145:106109. https://doi.org/10.1016/j.ijfatigue.2020.106109.
[31] Ma X, Zhai H, Song L, Zhang W, Hu Y, Zhang Q. *In situ* study on plastic deformation mechanism of $Al_{0.3}$CoCrFeNi high-entropy alloys with different microstructures. Mater Sci Eng A 2022;857:144134. https://doi.org/10.1016/j.msea.2022.144134.
[32] Bian N, Li F, Du H, Niu W, Chen Z. Effect mechanism of texture orientation on mechanical properties and Hall-Petch relationship of CVCDE AZ31 magnesium alloy via crystal plastic finite element method (CPFEM). J Alloys Compd 2022;923:166248. https://doi.org/10.1016/j.jallcom.2022.166248.
[33] Li W, Wang L, Zhou B, Liu C, Zeng X. Grain-scale deformation in a Mg−0.8 wt% Y alloy using crystal plasticity finite element method. J Mater Sci Technol 2019;35:2200–6. https://doi.org/10.1016/j.jmst.2019.04.030.
[34] Asgharzadeh A, Nazari Tiji SA, Park T, Pourboghrat F. Prediction of softening kinetics and recrystallization texture in non-isothermally annealed bulged tubes using CPFEM and CA models. Mater Sci Eng A 2022;832:142308. https://doi.org/10.1016/j.msea.2021.142308.
[35] Jiang M, Fan Z, Kruch S, Devincre B. Grain size effect of FCC polycrystal: a new CPFEM approach based on surface geometrically necessary dislocations. Int J Plast 2022;150:103181. https://doi.org/10.1016/j.ijplas.2021.103181.

[36] Asim UB, Siddiq MA, Kartal ME. A CPFEM based study to understand the void growth in high strength dual-phase titanium alloy (Ti-10V-2Fe-3Al). Int J Plast 2019;122:188–211. https://doi.org/10.1016/j.ijplas.2019.07.002.
[37] Zhang D, Li H, Guo X, Yang Y, Yang X, Feng Z. An insight into size effect on fracture behavior of Inconel 718 cross-scaled foils. Int J Plast 2022;153:103274. https://doi.org/10.1016/j.ijplas.2022.103274.
[38] Zhang J, Li X, Xu D, Teng C, Wang H, Yang L, Ju H, Xu H, Meng Z, Ma Y, Wang Y, Yang R. Phase field simulation of the stress-induced α microstructure in Ti–6Al–4V alloy and its CPFEM properties evaluation. J Mater Sci Technol 2021;90:168–82. https://doi.org/10.1016/j.jmst.2020.12.085.
[39] Iftikhar CMA, Brahme A, Inal K, Khan AS. An evolution of subsequent yield loci under proportional and non-proportional loading path of 'as-received' extruded AZ31 magnesium alloy: experiments and CPFEM modeling. Int J Plast 2022;151:103216. https://doi.org/10.1016/j.ijplas.2022.103216.
[40] Muhammad W, Brahme AP, Ali U, Hirsch J, Engler O, Aretz H, Kang J, Mishra RK, Inal K. Bendability enhancement of an age-hardenable aluminum alloy: part II — multiscale numerical modeling of shear banding and fracture. Mater Sci Eng A 2019;754:161–77. https://doi.org/10.1016/j.msea.2019.03.050.
[41] Cao J, Zhuang W, Wang S, Lin J. Development of a VGRAIN system for CPFE analysis in micro-forming applications. Int J Adv Manuf 2010;47:981–91. https://doi.org/10.1007/s00170-009-2135-3.
[42] Guo N, Wang J, Sun CY, Zhang YF, Fu MW. Analysis of size dependent earing evolution in micro deep drawing of TWIP steel by using crystal plasticity modeling. Int J Mech Sci 2020;165:105200. https://doi.org/10.1016/j.ijmecsci.2019.105200.
[43] Adzima F, Balan T, Manach PY. Springback prediction for a mechanical micro connector using CPFEM based numerical simulations. Int J Mater Form 2020;13:649–59. https://doi.org/10.1007/s12289-019-01503-5.
[44] Tong X, Zheng JY, Fu MW. Numerical and experimental study of the size effect on deformation behavior and quality of microembossed multi-channel structures. J Manuf Process. 2022;78:363–75. https://doi.org/10.1016/j.jmapro.2022.04.047.
[45] Leicht M, Rohrmoser A, Kraus M, Merklein M. Investigation of the influence of material and sheet thickness on a three-stage process chain for cold forming of micro gears with a module of 0.1mm. IOP Conf Ser Mater Sci Eng 2022;1270:012094. https://doi.org/10.1088/1757-899X/1270/1/012094.
[46] Arora A, Pathak A, Juneja A, Shakkarwal P, Kumar R. Design & analysis of progressive die using SOLIDWORKS. Mater Today Proc 2022;51:956–60. https://doi.org/10.1016/j.matpr.2021.06.335.
[47] Wang Z, Zhang J, Xu Z, Zhang J, Hu H, Li G, Zhang H, Hartmaier A, Fang F, Yan Y, Sun T. Crystal plasticity finite element modeling and simulation of diamond cutting of polycrystalline copper. J Manuf Process 2019;38:187–95. https://doi.org/10.1016/j.jmapro.2019.01.007.
[48] Liu Q, Roy A, Tamura S, Matsumura T, Silberschmidt VV. Micro-cutting of single-crystal metal: finite-element analysis of deformation and material removal. Int J Mech Sci 2016;118:135–43. https://doi.org/10.1016/j.ijmecsci.2016.09.021.
[49] Liu LY, Yang QS, Liu X, Nian XC. Crystal cracking of grain-gradient aluminum by a combined CPFEM-CZM method. Eng Fract Mech 2021;242:107507. https://doi.org/10.1016/j.engfracmech.2020.107507.
[50] Phan VT, Zhang X, Li Y, Oskay C. Microscale modeling of creep deformation and rupture in Nickel-based superalloy IN 617 at high temperature. Mech Mater 2017;114:215–27. https://doi.org/10.1016/j.mechmat.2017.08.008.
[51] Xu XP, Needleman A. Void nucleation by inclusion debonding in a crystal matrix. Modell Simul Mater Sci Eng 1993;1:111. https://doi.org/10.1088/0965-0393/1/2/001.
[52] Clayton JD, McDowell DL. Homogenized finite elastoplasticity and damage: theory and computations. Mech Mater 2004;36:799–824. https://doi.org/10.1016/j.mechmat.2003.08.001.
[53] Clayton JD. Dynamic plasticity and fracture in high density polycrystals: constitutive modeling and numerical simulation. J Mech Phys Solids 2005;53:261–301. https://doi.org/10.1016/j.jmps.2004.06.009.
[54] Zhao N, Wang W, Liu Y. Intergranular mechanical behavior in a blade groove-like component by crystal plasticity model with cohesive zone model. Eng Fract Mech 2018;201:196–213. https://doi.org/10.1016/j.engfracmech.2018.06.031.
[55] Ghodrati M, Ahmadian M, Mirzaeifar R. Three-dimensional study of rolling contact fatigue using crystal plasticity and cohesive zone method. Int J Fatigue 2019;128:105208. https://doi.org/10.1016/j.ijfatigue.2019.105208.
[56] Yalçinkaya T, Özdemir İ, Firat AO. Inter-granular cracking through strain gradient crystal plasticity and cohesive zone modeling approaches. Theor Appl Fract Mech 2019;103:102306. https://doi.org/10.1016/j.tafmec.2019.102306.
[57] Lyu D, Fan H, Li S. A hierarchical multiscale cohesive zone model and simulation of dynamic fracture in metals. Eng Fract Mech 2016;163:327–47. https://doi.org/10.1016/j.engfracmech.2016.06.005.
[58] Kalidindi SR. Incorporation of deformation twinning in crystal plasticity models. J Mech Phys Solids 1998;46:267–90. https://doi.org/10.1016/S0022-5096(97)00051-3.
[59] Cai W, Sun C, Wang C, Qian L, Li Y, Fu MW. Modelling of the intergranular fracture of TWIP steels working at high temperature by using CZM–CPFE method. Int J Plast 2022;156:103366. https://doi.org/10.1016/j.ijplas.2022.103366.
[60] Salem AA, Kalidindi SR, Semiatin SL. Strain hardening due to deformation twinning in α-titanium: constitutive relations and crystal-plasticity modeling. Acta Mater 2005;53:3495–502. https://doi.org/10.1016/j.actamat.2005.04.014.
[61] Kalidindi S R. Modeling anisotropic strain hardening and deformation textures in low stacking fault energy fcc metals. Int J Plast 2001;17:837–60. https://doi.org/10.1016/S0749-6419(00)00071-1.
[62] Lu M, Wang F, Zeng X, Chen W, Zhang J. Cohesive zone modeling for crack propagation in polycrystalline NiTi alloys using molecular dynamics. Theor Appl Fract Mech 2020;105:102402. https://doi.org/10.1016/j.tafmec.2019.102402.
[63] Jia N, Roters F, Eisenlohr P, Kords C, Raabe D. Non-crystallographic shear banding in crystal plasticity FEM simulations: example of texture evolution in α-brass. Acta Mater 2012;60:1099–115. https://doi.org/10.1016/j.actamat.2011.10.047.
[64] Chiarodo R, Spain I, Bolsaitis P. Elastic constants and their pressure derivatives of α-brass single crystals. J Phys Chem Solids 1974;35:762–4. https://doi.org/10.1016/S0022-3697(74)80234-9.
[65] Li K, Yu B, Misra RDK, Han G, Tsai YT, Shao CW, Shang CJ, Yang JR, Zhang ZF. Strain rate dependence on the evolution of microstructure and deformation mechanism during nanoscale deformation in low carbon-high Mn TWIP steel. Mater Sci Eng A 2019;742:116–23. https://doi.org/10.1016/j.msea.2018.11.006.
[66] Wang YJ, Ru CQ. Determination of two key parameters of a cohesive zone model for pipeline steels based on uniaxial stress-strain curve. Eng Fract Mech 2016;163:55–65. https://doi.org/10.1016/j.engfracmech.2016.06.017.
[67] Koster W., Rauscher W. Relations between the modulus of elasticity of binary alloys and their structure 1951. NACA-TM-1321.
[68] Kumar R, Misra A. Some basic aspects of electromagnetic radiation emission during plastic deformation and crack propagation in Cu–Zn alloys. Mater Sci Eng A 2007;454-455:203–10. https://doi.org/10.1016/j.msea.2006.11.011.
[69] Yan H, Zhao X, Jia N, Zheng Y, He T. Influence of shear banding on the formation of brass-type textures in polycrystalline FCC metals with low stacking fault energy. J Mater Sci Technol 2014;30:408–16. https://doi.org/10.1016/j.jmst.2013.11.010.
[70] Li L, Liu W, Qi F, Wu D, Zhang Z. Effects of deformation twins on microstructure evolution, mechanical properties and corrosion behaviors in magnesium alloys - a review. J Magnes Alloys 2022;10:2334–53. https://doi.org/10.1016/j.jma.2022.09.003.
[71] Praveen KG, Kurra S. Analysis of deformation behavior in various incremental tube forming processes. Mater Manuf Process 2021;36:1631–41. https://doi.org/10.1080/10426914.2021.1926493.
[72] Jia BB, Chen G, Wang WW, Shen Y, Gu Y. Deformation characteristics and forming force limits of multi-point forming with individually controlled force–displacement. Int J Adv Manuf 2022;123:1565–76. https://doi.org/10.1007/s00170-022-10236-w.
[73] Zhao Z, Li Y, Liu C, Chen Z, Chen J, Wang L. A subsequent-machining-deformation prediction method based on the latent field estimation using deformation force. J Manuf Syst 2022;63:224–37. https://doi.org/10.1016/j.jmsy.2022.03.012.
[74] Phillips WL, Armstrong RW. The strain dependence of the flow stress-grain size relation for 70:30 brass. Metall Trans 1972;3:2571–7. https://doi.org/10.1007/BF02644231.
[75] Li D, Wang L, Li W. Effects of grain size from micro scale to nanoscales on the yield strain of brass under compressive and tensile stresses using a Kelvin probing technique. Mater Sci Eng A 2004;384:355–60. https://doi.org/10.1016/j.msea.2004.06.060.
[76] Hönnige J, Seow CE, Ganguly S, Xu X, Cabeza S, Coules H, Williams S. Study of residual stress and microstructural evolution in as-deposited and inter-pass rolled wire plus arc additively manufactured Inconel 718 alloy after ageing treatment. Mater Sci Eng A 2021;801:140368. https://doi.org/10.1016/j.msea.2020.140368.
[77] Zhou W, Yu J, Lu X, Lin J, Dean TA. A comparative study on deformation mechanisms, microstructures and mechanical properties of wide thin-ribbed sections formed by sideways and forward extrusion. Int J Mach Tools Manuf 2021;168:103771. https://doi.org/10.1016/j.ijmachtools.2021.103771.
[78] Shrivastava SC, Jonas JJ, Canova G. Equivalent strain in large deformation torsion testing : theoretical and practical considerations. J Mech Phys Solids 1982;30:75–90. https://doi.org/10.1016/0022-5096(82)90014-X.
[79] Zhou H, Cui H, Qin QH. Influence of ultrasonic vibration on the plasticity of metals during compression process. J Mater Process Technol 2018;251:146–59. https://doi.org/10.1016/j.jmatprotec.2017.08.021.
[80] Karami K, Blok A, Weber L, Ahmadi SM, Petrov R, Nikolic K, Borisov EV, Leeflang S, Ayas C, Zadpoor AA, Mehdipour M, Reinton E, Popovich VA. Continuous and pulsed selective laser melting of Ti6Al4V lattice structures: effect of post-processing on microstructural anisotropy and fatigue behaviour. Addit Manuf 2020;36:101433. https://doi.org/10.1016/j.addma.2020.101433.
[81] Zheng JY, Liu H, Fu MW. Size effects on process performance and product quality in progressive microforming of shafted gears revealed by experiment and numerical modeling. Adv Manuf 2023;11:1–20. https://doi.org/10.1007/s40436-022-00414-0.
[82] Qamar SZ, Chekotu JC, Al-Maharbi M, Alam K. Shape complexity in metal extrusion: definitions, classification, and applications. Arab J Sci Eng 2019;44:7371–84. https://doi.org/10.1007/s13369-019-03886-8.
[83] Balasundar I, Raghu T. Investigations on the extrusion defect – axial hole or funnel. Mater Des 2010;31:2994–3001. https://doi.org/10.1016/j.matdes.2010.01.027.
[84] Deng JH, Fu MW, Chan WL. Size effect on material surface deformation behavior in micro-forming process. Mater Sci Eng A 2011;528:4799–806. https://doi.org/10.1016/j.msea.2011.03.005.
[85] Su Y, Song R, Wang T, Cai H, Wen J, Guo K. Grain size refinement and effect on the tensile properties of a novel low-cost stainless steel. Mater Lett 2020;260:126919. https://doi.org/10.1016/j.matlet.2019.126919.
[86] Qin W, Li J, Liu Y, Kang J, Zhu L, Shu D, Peng P, She D, Meng D, Li Y. Effects of grain size on tensile property and fracture morphology of 316L stainless steel. Mater Lett 2019;254:116–9. https://doi.org/10.1016/j.matlet.2019.07.058.
[87] Liao J, Zeng X, Xue X. Surface quality analysis of AZ31B Mg alloy sheet in ultrasonic-assisted warm single-point incremental forming. Int J Adv Manuf 2022;118:1397–410. https://doi.org/10.1007/s00170-021-08045-8.